Received: 21 December 2021 | Revised: 10 October 2022 | Accepted: 14 November 2022

DOI: 10.1111/jmg.12704

ORIGINAL ARTICLE

Journal of METAMORPHIC GEOLOGY WILEY

Polyphase tectonic reworking of serpentinites and chlorite-tremolite-talc rocks (SW Spain) from the subduction forearc to intracontinental emplacement

Benito Ábalos | **Pablo Puelles** | **José Ignacio Gil Ibarguchi**

Departamento de Geología, Facultad de Ciencia y Tecnología, Universidad del País Vasco UPV/EHU, Bilbao, Spain

Correspondence
Benito Ábalos, Departamento de Geología, Facultad de Ciencia y Tecnología, Universidad del País Vasco UPV/EHU, P.O. Box 644, E-48080 Bilbao, Spain.
Email: benito.abalos@ehu.es

Funding information
Spanish Ministry of Economy, Industry and Competitiveness and the Fondo Europeo de Desarrollo Regional (MINECO/FEDER CGL2015-63530-P; UPV/EHU (GIU20/010 and GIU15/05)

Handling Editor: Dr. Katy Evans

Abstract

The petrostructural and geochronological study of a poorly known ultramafic unit from SW Spain (Badajoz–Córdoba belt) combined with previous structural data permits disclosure of a history of metasomatism, tectono-metamorphism, reworking and isotopic resetting related to a poly-orogenic evolution in different geodynamic scenarios. The heterogeneous ultramafic unit studied contains antigorite-serpentinites and metasomatized ultramafic rocks (chlorite-talc schists, tremolite-talc-chlorite rocks and magnesio-hornblende-chlorite rocks). Mantle-wedge serpentinization was followed by Si and Al pre- to syn-metamorphic/tectonic metasomatism in a subduction realm. Petrofabrics of selected lithologies reveal variable syn-metamorphic crystal-plastic deformation and recrystallization (assisted by other mechanisms) under relative high pressure, concomitant with the conditions recorded by neighbouring tectonic units that were later intruded by Ordovician granites. The resultant ensemble was reworked and isotopically reset much later in an intracontinental ductile shear zone. Syn- to late-tectonic apatite from chlorite-talc schists provides an anchored Tera–Wassenburg isochron radiometric age of 342.8 ± 12.2 Ma that provides evidence for the decoupling between isotopic systems and microstructures. The results are discussed from a twofold perspective: with regard to the likely tectonic context of this ophiolite (the current analogue of the Mariana forearc) and with regard to regional geological implications.

KEYWORDS
apatite dating, Cadomian, petrofabric, serpentinite, Variscan

1 | INTRODUCTION

Talc-, amphibole- and chlorite-rich ultramafic rocks have been reported as integral parts of dismembered serpentinite s.l. sheets in Phanerozoic metamorphic terranes worldwide (Boschi et al., 2006; Guillot et al., 2015; Hess, 1933). Usually, those rocks formed by metasomatism of serpentinite bodies during their regional metamorphic evolution in contact with silica-rich crustal rocks (Epstein et al., 2021). Notwithstanding, the talc,

calcic amphibole (tremolite) and chlorite assemblage can develop in other tectonic environments at a range of temperatures below 450°C after replacement of primary and secondary ultramafic-mafic oceanic rock minerals, catalyzed by hydrothermal fluids and/or seawater-rock interactions. Altered ultramafic rocks bearing such a mineral assemblage have been reported in diverse active tectonic settings, including extensional (mid-ocean ridges, oceanic core complexes, transform faults and Atlantic-type ocean-continent transitions; e.g. Boschi et al., 2006 and references therein) and convergent ones, such as forearcs and active subduction zones (Epstein et al., 2021; Reynard, 2013; Wang et al., 2009). Fossil examples of these settings can be identified as tectonic slices in orogenic continental domains (Aertgeerts et al., 2018; Ouadahi et al., 2022; Picazo et al., 2013; Wakabayashi, 2017), where they may exhibit a close spatial relationship with high-pressure (HP) metamorphic rocks.

European pre-Mesozoic massifs record a late Proterozoic-early Palaeozoic geodynamic cycle ('Cadomian' in the regional literature, between 645 and 475 Ma). It was related to the extinct micro-continent Avalonia and a late Proterozoic magmatic arc or orogen (Linnemann et al., 2014) that occupied peripheral positions in North Gondwana (e.g. Cambeses et al., 2017). Current relict segments of them show that they accommodated the southward subduction (in Ediacaran–Cambrian geographical coordinates) of an oceanic slab beneath North Gondwana at high latitudes of the southern hemisphere (Wu et al., 2020). The Ossa–Morena zone of the Iberian Massif formed part of the convergent plate margin and exposes large volumes of Cadomian meta-igneous and meta-sedimentary rocks (Eguíluz et al., 2000; López-Guijarro et al., 2008; Pereira et al., 2011), including subduction-related (forearc and arc) basic-ultrabasic igneous rocks for which a renewed interest resulted in recent publications by Arenas et al. (2018), Díez Fernández et al. (2019) and Sarrionandia et al. (2020). Variscan reworking (mid-late Palaeozoic) and lithospheric-scale lateral displacements affected the entire northern margin of Gondwana (e.g. von Raumer et al., 2015) and was localized in lithospheric-scale shear zones of the southern Iberian Massif (Ábalos & Cusí, 1995; Burg et al., 1981; Silva & Pereira, 2004), where the radiometric footprints of the Cadomian orogeny were reset (e.g. Quesada & Dallmeyer, 1994; Ribeiro et al., 1990).

In this article, we present an analytical strategy (involving mineral geochemical analyses, microstructural and lattice-preferred orientation determinations, and geochronological studies) suited to examination of metasomatized ultramafic rocks common in orogenic zones worldwide. Other analytical tools currently available might provide complementary data that could help in the future to deepen the knowledge of these rocks. The unit scrutinized corresponds to a serpentinite tectonic slice from the Badajoz–Córdoba shear zone of the southern Iberian Massif. So far, it remains poorly known and has been mostly overlooked in the geological literature (e.g. Azor et al., 2022; Díez Fernández et al., 2022). The serpentinite presents field relationships with dated metamorphic units and granite intrusions, heterogeneous mineral assemblages, and mineral fabric features that permit us to unravel a complex and fascinating history of metasomatism, metamorphism, deformation and isotopic resetting related to a poly-orogenic (Cadomian and Variscan) evolution.

2 | GEOLOGICAL CONTEXT

2.1 | The Badajoz–Córdoba shear zone from the Ossa–Morena zone

Late Proterozoic–Early Palaeozoic rocks of the Ossa–Morena zone (OMZ henceforth; Figure 1) consist of Cadomian basement overlain by Palaeozoic sedimentary and volcanic sequences (Eguíluz et al., 2000; Quesada, 1990). The former crops out along three belts. The southern

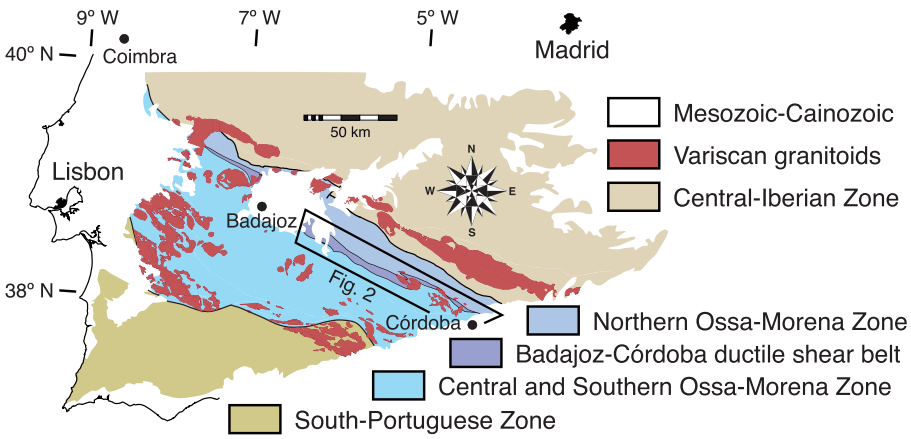

FIGURE 1 Geological sketch map of the southern Iberian massif showing a subdivision of the Ossa–Morena zone into northern and central/southern realms, separated by the Badajoz–Córdoba ductile shear belt (from which the rectangle area is shown in more detail in the Figure 2)

and central belts record low-pressure/high-temperature metamorphism, whereas the northern one, inclusive of the Badajoz–Córdoba shear zone (also known as Coimbra–Córdoba), records HP metamorphism (Ábalos et al., 1991; Arenas et al., 2020; López Sánchez-Vizcaíno et al., 2003) and contains igneous relics of a Cadomian arc (e.g. Bandrés et al., 2002, 2004; Quesada, 1990).

In the northern OMZ, geochemical and isotope signatures of >534 ± 4 Ma andesites (arc-tholeiites) and basaltic andesites (SiO_2-poor adakites) disclose a coeval continental active margin with an upper plate containing extended/hyper-extended transitional crust (Pin et al., 2002). During mature stages of the subduction, high-temperature/low-pressure metamorphism and coeval deformations took place in this active margin. These are thought of as being related to the moderate/steep (warm) subduction of relatively young ridge/transform oceanic lithosphere (Sarrionandia et al., 2020). Radiometric dating of basic-ultramafic metamorphosed protoliths and of intact calc-alkaline diorite and gabbro massifs allows for tracking the duration of plate convergence at least for 645–570 Ma (Bandrés et al., 2004; Sánchez-Lorda et al., 2014, 2016), that is, along *a* > 120 Ma time frame.

The Badajoz–Córdoba shear zone is a NW-SE trending intracontinental shear zone 30–40 km wide and 400 km long. It extends through Portugal and SW Spain (Figure 1) and contains both serpentinized ultramafic rocks and HP metamorphic rocks such as eclogite. Their outcrops form a strongly deformed band (i.e. a ductile shear belt) bounded by steeply dipping NW-SE strike-slip faults (Hornachos and Azuaga faults; Figure 2). This belt is organized into a thick allochthon (up to 6–8 km thickness measured normal to the regional foliation) of medium- to high-grade rocks emplaced onto a low-grade

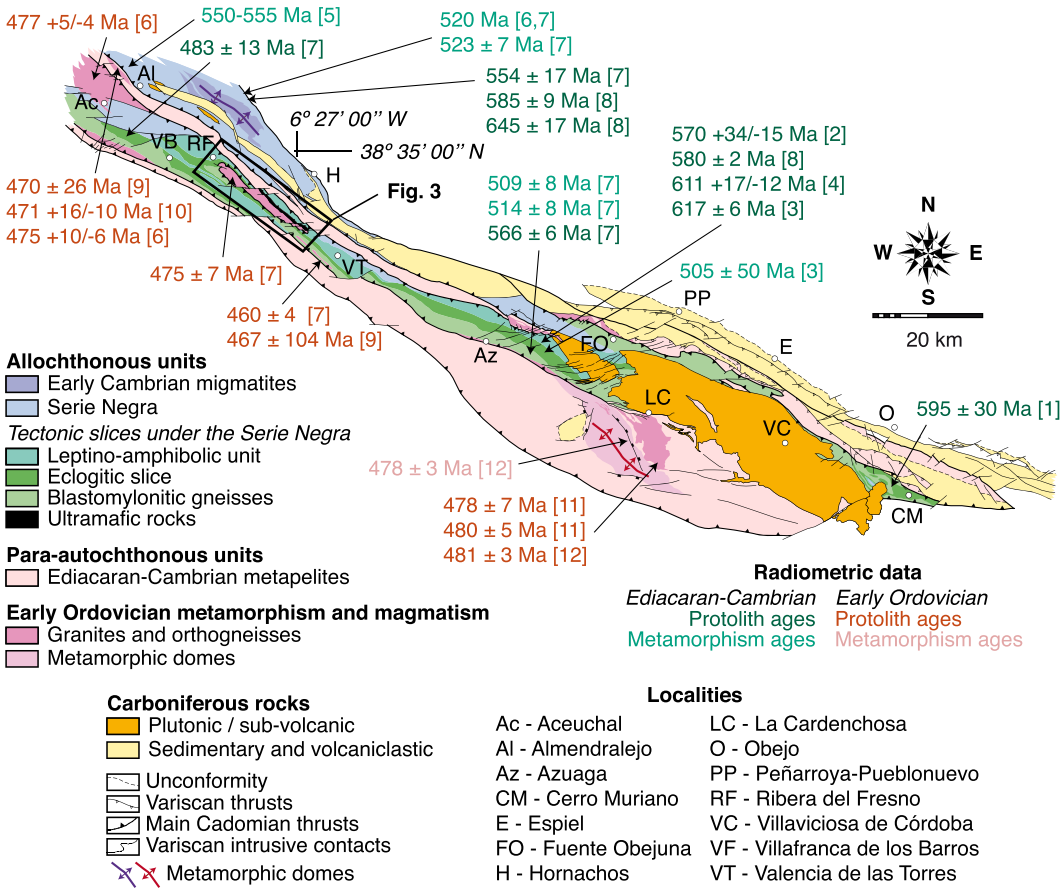

FIGURE 2 Geological sketch map of the Badajoz–Córdoba ductile shear zone including radiometric dating sampling sites that provided Ordovician and earlier (Ediacaran–Cambrian) protolith and metamorphism ages. Outcrops of a discontinuous and thin tertiary cover have been removed in order to highlight the distribution of the concealed geological units. See main text for further details. Geochronological references: [1] Bellon et al. (1979); [2] Schäfer et al. (1988); [3] Schäfer et al. (1989); [4] Schäfer et al. (1991); [5] Quesada and Dallmeyer (1994); [6] Ochsner (1993); [7] Ordóñez-Casado (1998); [8] Sánchez-Lorda et al. (2016); [9]; [10] Ochsner et al. (1992); [11] Azor et al. (2016); [12] Solís-Alulima et al. (2020). Localities: Ac, Aceuchal; Az, Azuaga; Al, Almendralejo; CM, Cerro Muriano; E, Espiel; FO, Fuente Obejuna; H, Hornachos; LC, La Cardenchosa; O, Obejo; PP, Peñarroya-Pueblonuevo; RF, Ribera del Fresno; VB, Villafranca de los Barros; VC, Villaviciosa de Córdoba; VT, Valencia de las Torres

para-autochthon (Apalategui et al., 1990). Ábalos (1990) mapped and categorized the metamorphic rocks of the allochthonous unit into five units (Figure 2) interpreted as tectonic slices. HP and high-grade metamorphism reached temperatures of 670–720 ± 30°C (gneisses) and 685 ± 25°C (eclogites), at pressures of 0.8–1.0 to >1.5 GPa (conventional geothermobarometry; Ábalos et al., 1991), or 550°C and 1.9 GPa (López Sánchez-Vizcaíno et al., 2003, pseudosection method applied to metabasites). Arenas et al. (2020) disclosed (by means of pseudosection modelling) P conditions close to the blueschist/eclogite facies transition of >2.0 GPa at ~525°C. These conditions exceed both the relatively high P and moderate T recorded by the metapelitic rocks of the underlying autochthonous unit (0.7–0.9 GPa and 500–575°C). The ensemble exhibits syn-metamorphic, continuous penetrative foliations (D1 fabrics) parallel to the lithological and thrust slice tectonic contacts, as well as SSW-verging recumbent folds with axes trending N160°E, subparallel to N160–200°E mineral and stretching lineations (see stereoplot in Figure 3). Shear-sense criteria provide a consistent pattern of south-directed tectonic emplacement directions of hangingwall blocks (Ábalos, 1992).

Radiometric dating of the eclogite facies metamorphism remains inconclusive so far. Schäfer (1990) and Schäfer et al. (1991) ascribed it to the Silurian (lower intercept age of zircon multi-grain analyses and Sm-Nd garnet age, respectively), but the attribution was later considered an artefact by Ordóñez-Casado (1998), as it might have resulted from analyzing mixed zircon domains of different ages, one of them being related to a 340 ± 13 Ma overprint. Metamorphic ages in the range 555–505 Ma were determined by Schäfer et al. (1989), Quesada and Dallmeyer (1994) and Ordóñez-Casado (1998) for other high-grade rocks (Figure 2). Other

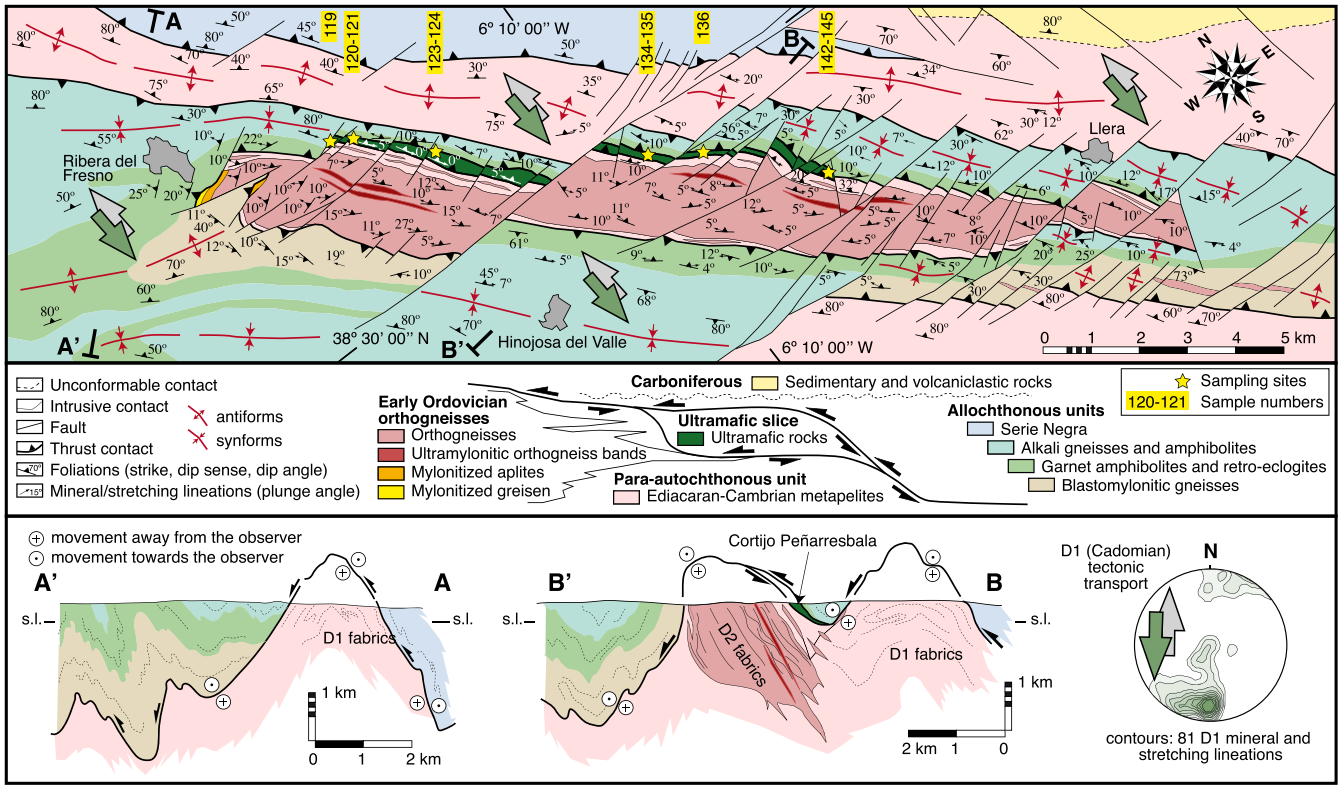

FIGURE 3 Geological map of the serpentinized ultramafic rock unit studied (in the context of the Ribera del Fresno tectonic window; Ábalos, 1989) and cross sections showing the geometrical relationships between a metamorphic allochthonous unit (containing gneisses and amphibolites with retrogressed eclogite relics), its para-autochthon (affected by a syn-tectonic greenschists facies metamorphism under relatively high pressure), the serpentinite slice sandwiched between them, and Early Ordovician intrusive rocks later transformed into orthogneisses. The stereoplot at the lower right (lower hemisphere, equal area projection) shows the attitude (contour shading in multiples of uniform distribution) of mineral and stretching lineations related to a deformation event (Cadomian D1) postdated by Ordovician granite intrusions and overprinted by ductile deformation fabrics that affected the whole ensemble (D2 Variscan overprint). Note the rotated geographical referential in the map with respect to that of the stereoplot, and that the S-ward inferred tectonic transport direction of hangingwall blocks (denoted by the top green and bottom grey arrow couples) is identical in both of them. Sampling sites for this study (yellow stars) and sample labels are tied by imaginary straight lines parallel to the map short edges

authors associate the HP metamorphism to the Variscan orogeny (e.g. Abati et al., 2018; Arenas et al., 2020; Azor, 1994, and references therein).

Granitoid rocks with 480–470 Ma protolith ages (Figure 2, and references contained there) did not register the HP metamorphism recorded by their country rocks (Ábalos, 1990). They form intrusive massifs with apophyses and satellite dykes emplaced along the mechanical anisotropies provided by D1 foliations and tectonic contacts. Country rock metamorphic xenoliths with D1 fabrics are also included near their rims (Ábalos, 1992; Azor et al., 2016; Simancas et al., 2000). These rocks show ductile deformation and were fully transformed into orthogneisses (with penetrative S–C fabrics) during a later D2 event dated in the interval 350–330 Ma (Abranches et al., 1979; Blatrix & Burg, 1981; García-Casquero et al., 1988; Ordóñez-Casado, 1998; Quesada & Dallmeyer, 1994).

D2 was synchronous with amphibolite to greenschist facies shear zone metamorphism (~500–350°C; Ábalos, 1992; Quesada & Dallmeyer, 1994) and can be attributed to the evolution of an intracontinental, lithospheric-scale ductile shear zone (Burg et al., 1981). D2 structures are dominated by regional steep foliations containing gently plunging N130–160°E stretching and mineral lineations with generalized sinistral wrench shear-sense criteria. The tens to hundreds of kilometres long wrench faults (with minor reverse fault components; e.g. Ábalos, 1992; Díez Fernández et al., 2021) that bound the Badajoz–Córdoba shear zone represent late brittle features resultant of reactivation of previous contacts and deformation localization.

2.2 | Serpentinite in the Badajoz–Córdoba shear zone

Involvement of the uppermost subcontinental lithospheric mantle in Cadomian tectonics of the Badajoz–Córdoba shear zone is evidenced by the occurrence of a fully serpentinized, 12 km long and 100–300 m thick ultramafic slice along the contact between the para-autochthonous and the allochthonous units described above (Figure 3). This slice has been repeatedly overlooked by most authors proposing geodynamic models for the Cadomian and Variscan tectonics of Iberia (e.g. Abati et al., 2018; Arenas et al., 2020; Azor et al., 2022; Díez Fernández et al., 2016, 2021; Díez Fernández & Arenas, 2015; Martínez-Catalán et al., 2021; Simancas et al., 2001; Solís-Alulima et al., 2020).

The written record on the discovery of serpentinites in the Badajoz–Córdoba shear zone and close domains of the northern OMZ is related to publication of the 1:50.000 maps of the area (Apalategui & Higueras, 1983; Arriola et al., 1983, b and c; Apalategui et al., 1988). These identified various heterogeneous serpentinite outcrops shortly before 1980 in two principal areas: two small "massifs" close to Calzadilla de los Barros (Cerro Cabrera, ~10 km^2 in outcrop area, and Cabeza Gorda, <2 km^2) and a ~12 km long and 100–300 m wide band cropping out between Ribera del Fresno and Llera (Figure 3). The latter was described independently also by Chacón and Velasco (1981) and Herranz (1984). Chacón (1979) did not map this unit in his Ph.D. dissertation, whereas Herranz (1984) illustrated his lithological and petrographic descriptions with a map of it, included as an appendix in his Ph.D. thesis, initiated in 1966 and published in 1985. Subsequent mapping and petrographic descriptions of the Ribera del Fresno–Llera serpentinites include only those of Ábalos (1989 and 1990), who related their outcrop to a tectonic window. Nonetheless, they are shown in the current digital version of the official 1:50.000 geological map of Spain (http://info.igme.es/visorweb/; latest consulted update, 26 February 2021).

The Calzadilla de los Barros serpentinites received special attention since their discovery. The preservation of (strongly serpentinized) peridotite lithotypes (including 70–90% olivine-bearing rocks that contain orthopyroxene with clinopyroxene exsolutions and chromite; cf. Arriola, Cueto, et al. (1983)) and the occurrence of podiform chromitites in them (Aguayo, 1985; Martos et al., 2010; Tornos et al., 2004) favoured their interpretation as Alpine-type ophiolite remnants, either emplaced as olistoliths (Apalategui et al., 1990) or as late Ediacaran obduction thrust sheets (Ábalos & Cusí, 1995; Arenas et al., 2018; Díez Fernández et al., 2019; Jiménez-Díaz, 2008; Jiménez-Díaz et al., 2009).

By contrast, the Ribera del Fresno–Llera serpentinite unit has not been studied in detail so far. Chacón and Velasco (1981) provided the first petrographic and mineral descriptions of these ultramafic rocks, which permitted them to infer a spinel facies orogenic lherzolite precursor. The authors referred to the unit as having an 'ophiolitoid' character and envisaged their tectonic emplacement in the context of a Cadomian suture without further structural or mapping support. Herranz (1985) interpreted these rocks as igneous ultramafic intrusives emplaced along a subvertical tectonic contact.

The Ribera del Fresno–Llera ultramafic rocks were visited (notably the so-called Cortijo de Peñarresbala outcrops) during two field trips in 1986 (Martínez-García et al., 1986) and 1987 (Apalategui & Quesada, 1987). The former preceded publication of the geological synthesis of pre-Mesozoic Iberia led by Dallmeyer and Martínez-García (1990), where Apalategui et al. (1990) interpreted those serpentinites as a thrust sheet (as also did

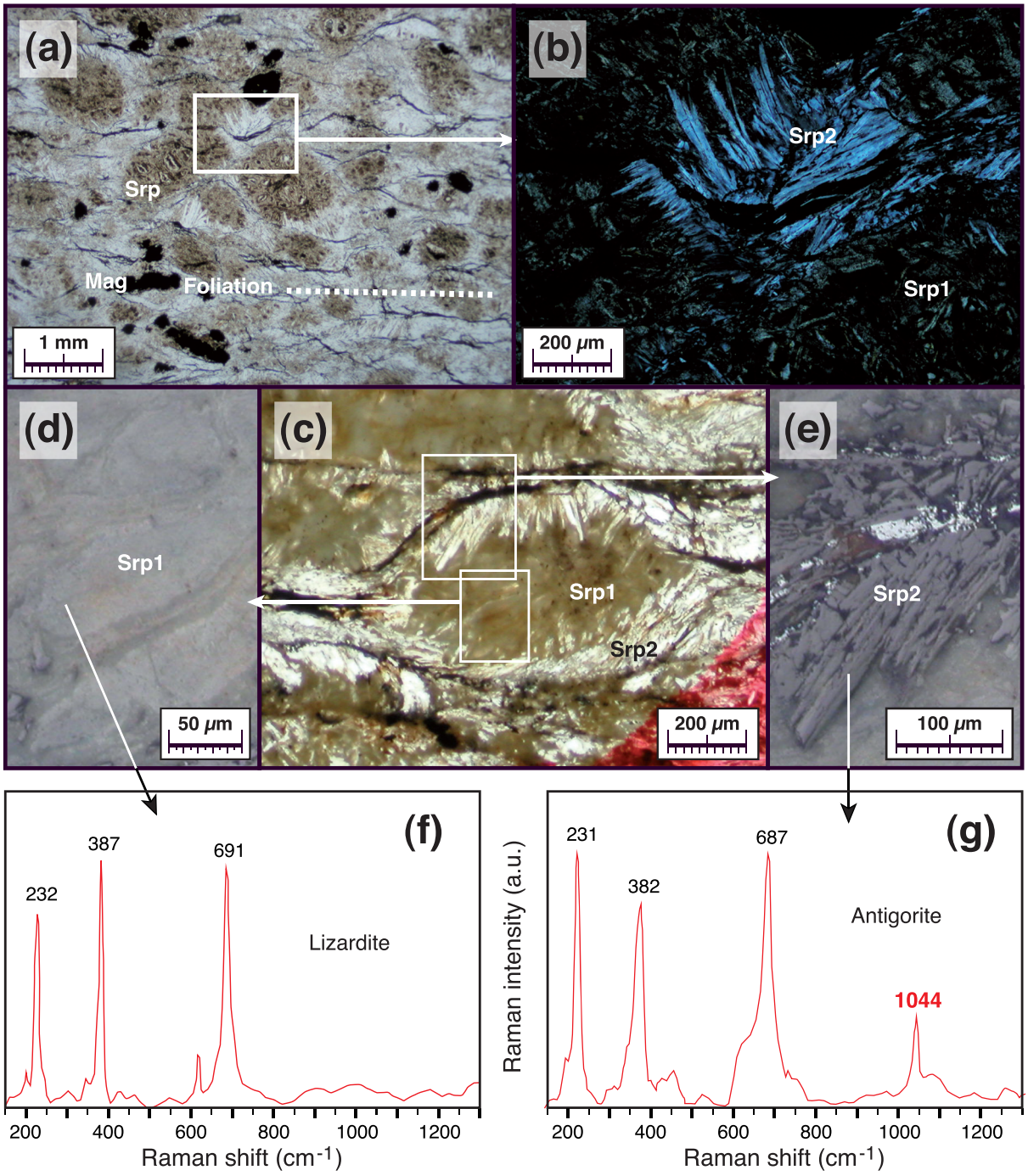

FIGURE 4 Optical microphotographs of representative microstructures of Type 1 serpentinites. (a) Plane polarized light microphotograph of a fully serpentinized peridotite showing sigmoidal serpentine (Srp) and magnetite (Mag) aggregates that contribute to define a penetrative foliation. (b) Magnification of the white rectangle area in (a) under crossed nicols showing a dark fine-grained serpentine matrix (Srp1) and a clear, larger, blade-like serpentine crystal aggregate (Srp2). (c) Optical microphotograph under polarized light of a sigmoidal serpentine porphyroclast system (also delineated by thin opaque mineral trails) with a dusty serpentine core (Srp1) and clear blade-like serpentine crystal aggregates (Srp2) defining a quarter microstructure. (d, e) Magnifications of the white rectangle areas in Figure 4c under crossed nicols and reflected light showing the location of the Raman spectroscopy laser incidence spots in the two serpentine mineral types recognized. (f, g) Resultant lizardite and antigorite Raman spectra with indications of the Raman shifts corresponding to the discriminating peaks (a.u.: arbitrary units of intensity). Mineral abbreviations after Whitney and Evans (2010)

Ábalos, 1989, 1990, 1992). By contrast, Azor et al. (1994) presented a revised regional study of the area (accompanied by a map) that overlooked the presence of these ultramafic rocks and merged the metamorphic rock variety of the area into a single "Central Unit". This ensemble has been subsequently taken as starting reference in several articles, books and maps of the area (e.g. Abati et al., 2018; Arenas et al., 2020; Azor et al., 1994; Díez Fernández et al., 2016, 2021; Díez Fernández & Arenas, 2015; Martínez-Catalán et al., 2021; Simancas et al., 2001; Solís-Alulima et al., 2020).

3 | METHODS

A detailed description of the methods used for rock-forming mineral identification (petrographic thin sections, X-ray diffraction, Raman spectroscopy), mineral geochemical analysis (electron-microprobe), determination of mineral petrofabric (electron back-scattered diffraction, EBSD) and apatite dating (laser ablation inductively coupled plasma mass spectrometry, LA-Q-ICPMS) are presented in the supporting information Appendix S1.

4 | PETROGRAPHY

The Ribera del Fresno–Llera ultramafic rocks consist of low- to medium-grade, variably foliated dark green metamorphic rocks and exhibit a remarkable mineralogical heterogeneity. Outcrops are scarce and the unit is usually weathered and covered by soils or agricultural land. This challenges recognition of a reliable areal distribution of lithotypes, with the exception of preponderance of foliated rocks along the basal and top contacts of the unit. Table S1 contains a brief lithological description and the geographic coordinates of the samples used in this study (Figure 3).

In the samples studied, the primary ultramafic mineral assemblage was almost totally erased by subsequent alterations. Chacón and Velasco (1981) described relict olivine (a 50% modal proportion of Fo_{40}; this composition is a rough estimation of the authors after measuring the 2 V angle between the optic axes of olivine with a U-stage, and probably is wrong), pargasitic amphibole (20% in modal proportion), rare clinopyroxene, and relict deep green spinel (hercynite; all optically determined). These characteristics would point to a spinel facies orogenic lherzolite precursor, though so far has not been confirmed. Arc peridotites might be considered a candidate, among the various possibilities that exist. As regards the serpentinite mineral phases, Chacón and Velasco (1981) reported antigorite, chrysotile (asbesto), chlorite and magnetite.

Petrographically, serpentine (lizardite, antigorite, chrysotile, greenalite and amesite), chlorite (clinochlore; structural formulae calculated after Jacobson, 1989), amphibole (actinolite, tremolite and magnesio-hornblende; Holland & Blundy, 1994; Dale et al., 2000), talc (Pognante, 1989), apatite, dolomite, magnetite, ilmenite (Dymek et al., 1988), hematite and goethite are the mineral constituents identified in this study (Table S2). The relationships they exhibit with respect to penetrative and localized deformation microstructures (foliations and variably deformed veins) suggest various growth stages. This is the case of opaque mineral trails and disseminations, which may delineate sigmoidal porphyroclast systems, show shape fabrics parallel to the foliation (Figure 4), infill mildly reworked fibrous veins (Figures 5 and 6), or form precipitates along sheet-silicate exfoliation planes and rims. Magnetite is a common opaque mineral phase in most samples and confers them a variably intense magnetism (hand-sized rock samples deflect the compass needle).

The studied samples have been divided into four types: (1) foliated ultramafic rocks dominated by sheet silicates, mainly serpentinites (Type 1 serpentinites; Figure 4); (2) foliated serpentinite with abundant veins and secondary infillings (Type 2 serpentinites; Figure 5); (3) poorly foliated serpentinites with centimetre-sized pseudomorphs after idiomorphic crystals of amphibole (Type 3 serpentinites; Figures 6–8); and (4) mineralogically more heterogeneous metamorphic ultramafic rocks including chlorite-talc schists (Figures 9 and 10), tremolite-talc-chlorite rocks (Figure 11) and magnesio-hornblende-chlorite rocks (Figure 12). The mineralogically heterogeneous metamorphic ultramafic rocks are less frequent than serpentinite, though potentially are of great petrological interest.

4.1 | Serpentinite types

Type 1 serpentinites (Figure 4) contain serpentine with the characteristic mesh textures (Wicks & Whittaker, 1977) as well as fine-grained aggregates of sub-idiomorphic blades and fibrous aggregates. Microstructures vary from pseudomorphic to foliated and are typical of a fully serpentinized peridotite. Sigmoidal serpentine porphyroclast systems (with internal quarter microstructures) and minute magnetite grain trails contribute to define a C–S fabric and a penetrative foliation (Figure 4a–c). XRD was unable to discriminate between antigorite and lizardite in this type of samples. However, it confirmed the presence of two (and even three)

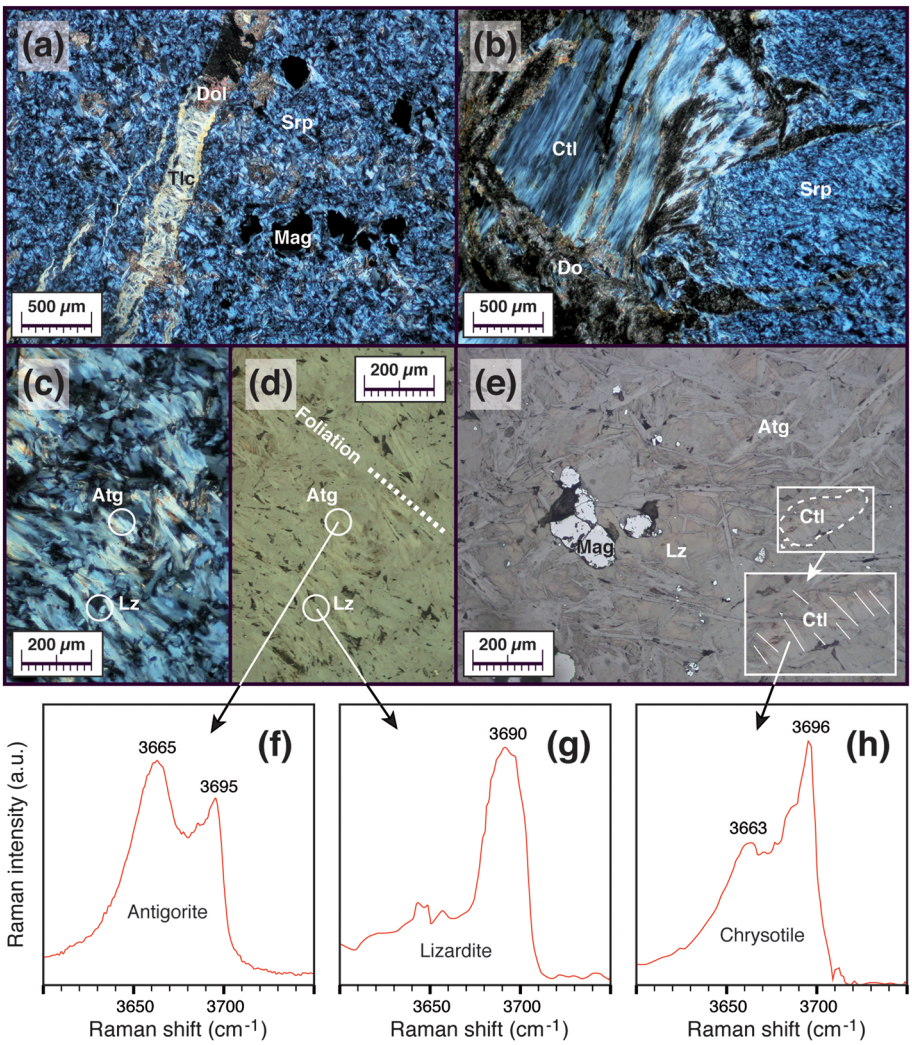

FIGURE 5 Optical microphotographs of representative microstructures of Type 2 serpentinite. (a) Optical microphotograph under crossed nicols of a serpentinite traversed by a polymineralic vein that contains antitaxial fibrous talc (Tlc), dolomite (Do) and magnetite (Mag) infillings. The surrounding medium consists of serpentine (Srp) and magnetite (Mag). (b) Optical microphotograph under crossed nicols of a complex vein mineral infilling (to the left of the image) including dolomite and fibrous serpentine (likely chrysotile, Ctl) that contrasts with the habit of host rock serpentine (to the right). (c) and (d) Optical microphotographs under transmitted parallel and reflected light with crossed nicols, respectively, showing the microstructure of the foliated serpentinite matrix, containing antigorite (Atg) and lizardite (Lz). (e) Optical microphotographs under reflected parallel light of the serpentinite matrix showing serpentine minerals with three habits, namely a fine-grained darker groundmass, reflective blade-like crystals with various orientations, and ellipsoidal clear domains (see enlarged view of the rectangle inset) with an internal fibrous microstructure. (f–h) Complementary to the 150–1300 cm^{-1} Raman spectral windows (not shown), the 3600–3750 cm^{-1} window spectra obtained for the specific sites (arrow tails) pinpointed in Figure 5c–e permit to identify as lizardite the serpentine from the fine-grained darker groundmass (Lz), as antigorite the reflective blade-like crystals (Atg), and as a serpentine different from both lizardite and antigorite for the case of the domains with an internal fibrous microstructure. Such a serpentine is tentatively interpreted as chrysotile (Ctl). In the Raman spectra, the Raman shifts corresponding to the discriminating peaks are indicated by number labels (a.u.: arbitrary units of intensity). Mineral abbreviations after Whitney and Evans (2010)

coexisting serpentine phases. The preliminary petrographic identification of lizardite and antigorite (occasionally accompanied by the Fe-rich greenalite serpentine) was corroborated with Raman spectroscopy. The optically darker (under reflected polarized light) and finer-grained serpentine matrix (Srp1 in Figure 4c, d) corresponds to lizardite, whereas the clear, larger, blade-like serpentine crystal aggregates from the quarter structures (Srp2 in Figure 4c, e) correspond to antigorite (note the absence or the presence of the discriminating 1044 cm^{-1} Raman spectra peaks in Figure 4f and g, respectively). The occurrence of antigorite among the

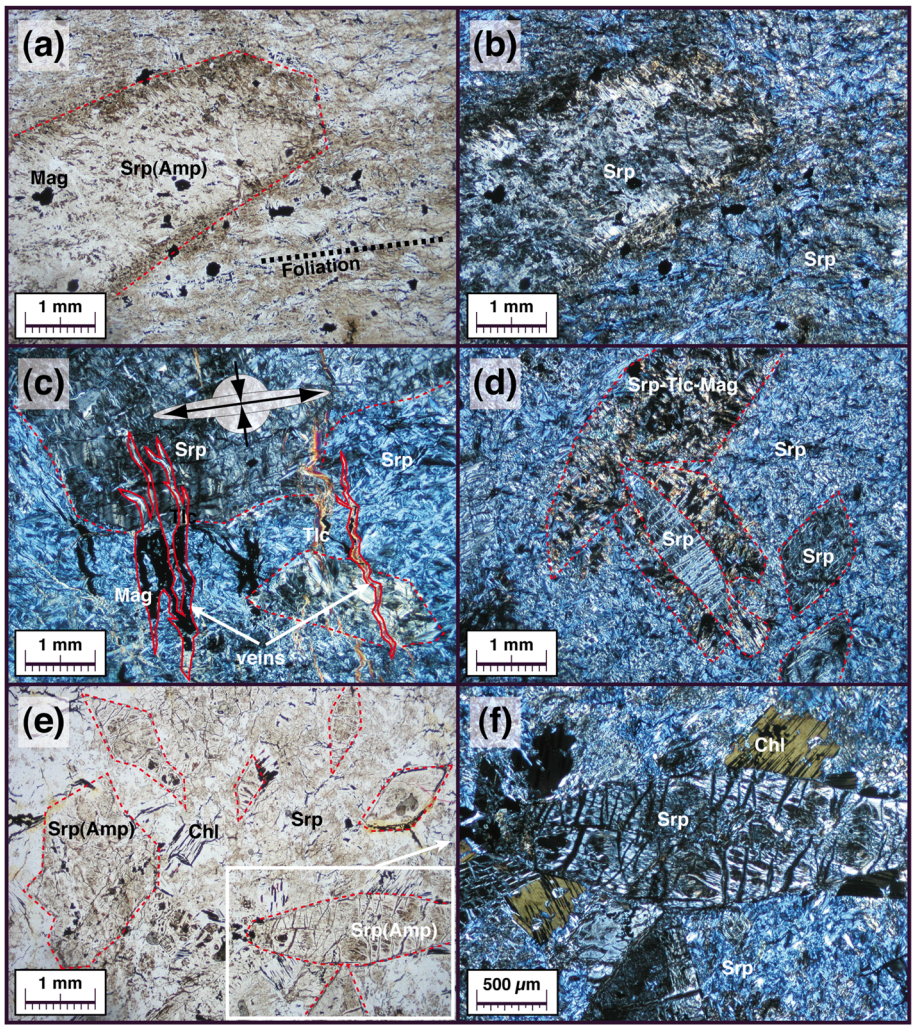

FIGURE 6 Optical microphotographs of representative microstructures of Type 3 serpentinites. (a, b) Optical microphotographs under parallel (a) and crossed nicols (b) showing the microstructure of a fully serpentinized amphibole (Amp) crystal ghost and of a distinct foliated serpentine matrix surrounding it. Serpentine (Srp) exhibits two contrasting appearances and is associated to magnetite (Mag). (c) Optical microphotograph under crossed nicols of amphibole ghosts (delimited with red dashed lines) altered to serpentine with a mesh texture and surrounded by a texturally distinct serpentine matrix. The ensemble is cut across by a set of parallel veins (delimited by red traces) infilled with serpentine, magnetite (Mag) and talc (Tlc). The veins are geometrically related to the foliation strain field (see the undeformed circle and the deformed strain ellipse, with shortening and elongation direction arrows, at the top of the image) and denote extension along the foliation postdating the ghost crystal serpentinization. The veins were subsequently shortened under the same strain field, which permits to interpret them as syn-tectonic with respect to the foliation. (d) Optical microphotograph under crossed nicols of an amphibole ghost crystal cluster (euhedral crystals delimited with red dashed lines) altered to serpentine, talc and magnetite. Serpentinization along amphibole host cleavage planes is distinct from that along fractures perpendicular to crystal elongations, which usually show vein habits with median lines. (e) Plane polarized light microphotograph of a fully serpentinized peridotite with amphibole ghosts (delimited with red dashed lines) and euhedral chlorite (Chl) crystals containing opaque mineral alterations along their cleavage planes. (f) Magnification under crossed nicols of the white rectangled area from Figure 6e. Note the contrasting appearance of serpentine (Srp) in amphibole crystal ghosts (with a mesh microstructure) and in the surrounding matrix (more homogeneous and fine-grained). See text for further details. Mineral abbreviations after Whitney and Evans (2010)

serpentine minerals points to a higher-T (and P) metamorphic origin for the syn-metamorphic microstructures that this mineral exhibits, as compared to previous serpentinization stages recorded by lizardite (Aupart et al., 2021; Guillot et al., 2015). Schwartz et al.'s (2013) temperature-defined transition between lizardite and antigorite suggests that antigorite crystallization would have occurred in these rocks under temperatures between 320–390 and 460°C.

Type 2 serpentinites (Figure 5) are characterized by the presence of polymineralic veins traversing the serpentinite bodies. Antitaxial fibrous talc, dolomite and

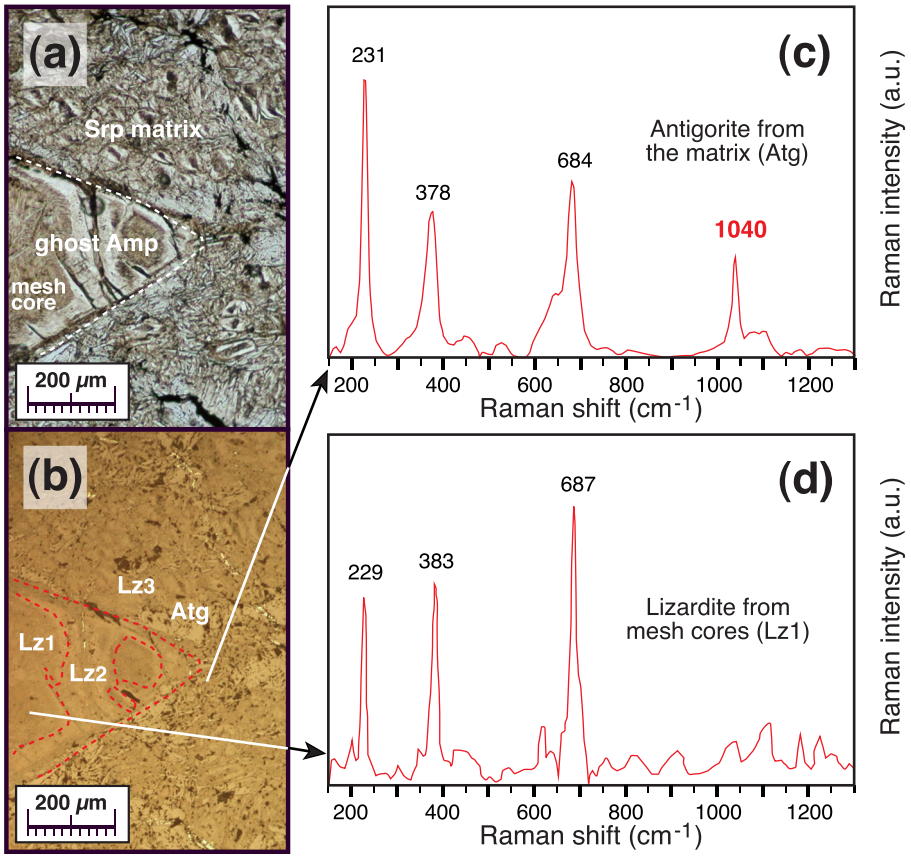

FIGURE 7 Optical microphotographs of representative microstructures of Type 3 serpentinites. (a, b) Optical microphotographs under transmitted parallel (a) and reflected light with crossed nicols (b) showing the microstructure of a serpentinized amphibole (Amp) crystal ghost and of the matrix surrounding it. The ghost amphibole exhibits a mesh texture with darker serpentine cores included by a network of colourless serpentine veins and rims. The fine-grained surrounding matrix is made as well of two serpentine types including more reflective blade-like crystals embedded in a darker groundmass. The Raman spectra obtained for the specific sites (arrow tails) shown in Figure 7b permit to identify as antigorite (c) the reflective blade-like crystals (Atg) and as lizardite (d) the serpentine from both the mesh cores (Lz1) and rims (Lz2), the remaining matrix corresponding to a third lizardite type (Lz3). In the spectra (c, d), the Raman shifts corresponding to the discriminating peaks are indicated with number labels (a.u.: arbitrary units of intensity). Mineral abbreviations after Whitney and Evans (2010)

magnetite (Figure 5a) are the main secondary vein infillings, although association of dolomite and fibrous serpentine with a different habit from the serpentine in the matrix may also occur (Figure 5b). The veins are geometrically related to the foliation strain field, denoting extension along the foliation and a slight shortening across it (Figure 5c), suggestive of a syn-tectonic character with respect to the foliation. The serpentinite matrix consists of serpentine and magnetite crystal aggregates showing a continuous and penetrative foliation at the microscale. Matrix serpentine minerals exhibit three habits (Figure 5c–e): a fine-grained and optically darker groundmass, reflective blade-like crystals with various orientations that track the rock foliation, and ellipsoidal clear domains with an internal fibrous microstructure. Fibrous serpentine aggregates postdate serpentinite fabrics in these rocks (Figure 5e). The coexistence of three serpentine phases is supported by XRD and was corroborated with the help of Raman spectroscopy (Figure 5f–h). The 3600–3750 cm^{-1} Raman spectral windows (complementary to the 150–1300 cm^{-1}) suggest lizardite as the serpentine from the dark matrix groundmass, antigorite as syn-tectonic blade-like matrix crystals, and chrysotile as the domains with an internal fibrous microstructure.

Type 3 serpentinites contain centimetre-sized pseudomorphs after idiomorphic crystals of amphibole embedded in a dark serpentine-chlorite-talc matrix (Figures 6–8). Amphibole pseudomorphs show light colour in hand specimens and are completely serpentinized (Figure 6). In hand specimen sawed sections the orientation of their largest dimension ranges between random and slightly oriented. Derivation of some porphyrocrystals of this type after pyroxene cannot be discarded, taking into account the external shape and exfoliation

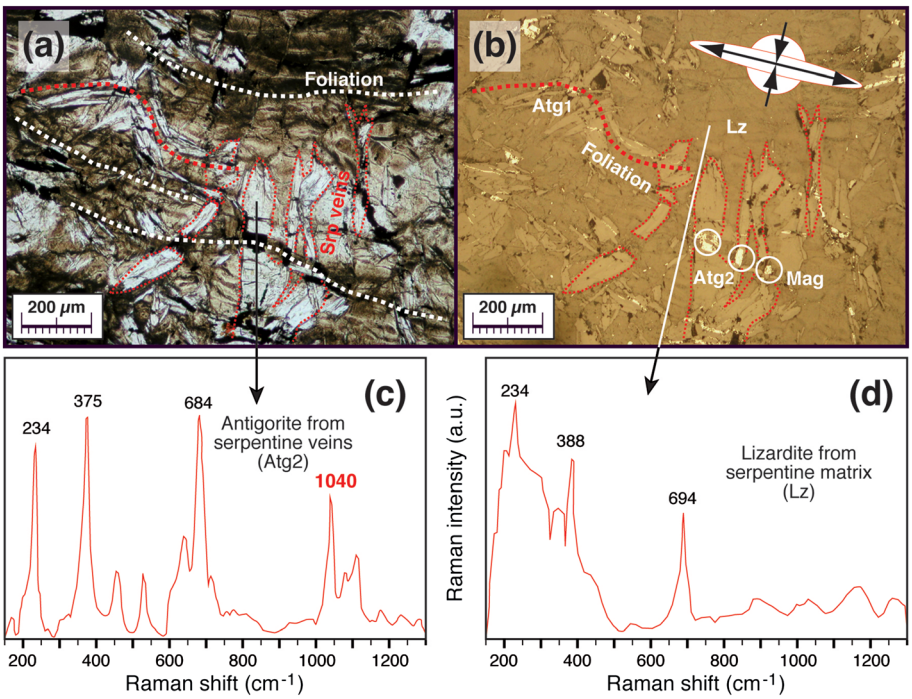

FIGURE 8 Optical microphotographs of representative microstructures of the matrix of Type 3 serpentinites. (a, b) Optical microphotographs under transmitted parallel (a) and reflected light with crossed nicols (b) showing the microstructure a fine-grained, banded/foliated, darker background including more reflective blade-like crystals. The latter exhibit two habits: large aspect ratio crystals that contribute to define the rock background foliation and smaller aspect ratio crystals elongated at high angles to it. This arrangement is interpreted as related to two generations of reflective blade-like crystals, an older one along the foliation and a slightly younger one grown in extensional veins geometrically related to the foliation strain field (see the undeformed circle and the deformed strain ellipse, with shortening and elongation direction arrows, at the top right of Figure 8b. A trail of magnetite fragments (Mag, encircled in Figure 8b) also denotes extension along the foliation direction. (c and d) The Raman spectra obtained for the specific sites (arrow tails) shown in Figure 8a and b permit to identify as lizardite (Lz) the serpentine from the background matrix and as antigorite the reflective blade-like crystals that define the foliation (Atg1) and fill extension veins (Atg2). In the Raman spectra, the Raman shifts corresponding to the discriminating peaks are indicated with number labels (a.u.: arbitrary units of intensity). Mineral abbreviations after Whitney and Evans (2010)

organizations of a few rare examples. Some amphibole pseudomorphs may exhibit zoned microstructures with darker/clouded thin rims and clear cores (Figure 6a, b). Their serpentinization progressed along grain boundaries (Figure 6a, b), microfractures and along cleavage planes (Figure 6c–f). Serpentine formed along microfractures exhibit central partings that are absent along cleavages and combine to produce characteristic mesh textures (Wicks & Whittaker, 1977). Darker serpentine mesh cores are surrounded by a network of colourless serpentine veins and rims (Figure 7a). The fine-grained surrounding matrix is made as well of two serpentine types including brighter blade-like crystals embedded in a darker groundmass (Figure 7b). XRD enabled us to identify four serpentinite mineral phases including greenalite and the rare Al-rich amesite. The Raman spectra obtained for the specific serpentine petrographic types described above (Figure 7c, d) identify lizardite as the serpentine from both the mesh cores and rims (Lz1 and Lz2 in the Figure 7b) and antigorite as the tiny blade-like crystals of the surrounding matrix, coexisting with a third lizardite type (Lz3 in Figure 7b). Certain serpentinite matrix domains provide additional microstructural details on the syn-tectonic growth of antigorite (Figure 8a, b) after ultramafic rock protolith primary serpentinization (by lizardite; cf. Figure 8c, d). Two antigorite generations occur: (1) large aspect ratio grains that define the foliation (Atg1) and (2) smaller aspect ratio crystal clusters (Atg2) that cross-cut the foliation (Figure 8a, b). This arrangement is interpreted as related to two antigorite generations, namely a slightly older one (Atg1 in Figure 8b) along the foliation and a slightly younger one (Atg2 in Figure 8b) grown in extensional veins perpendicular to it. The strain field consistent with these geometrical relationships is congruent with antigorite syn-tectonic growth during progressive deformation and is also tracked by magnetite fragments extended along the foliation direction (Figure 8b).

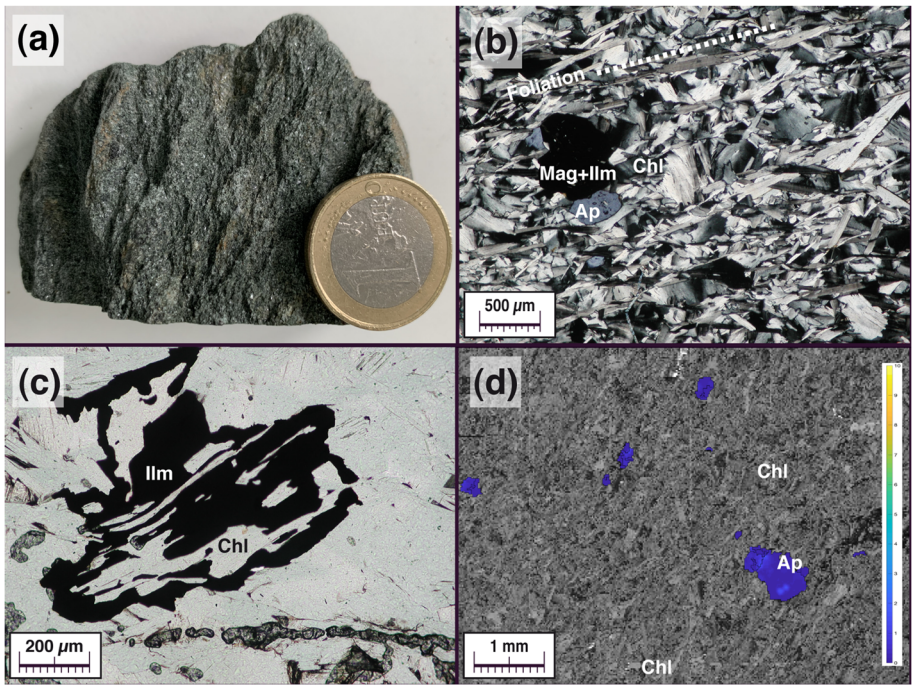

FIGURE 9 Optical microphotographs of chlorite-talc schists from mineralogically heterogeneous metamorphic ultramafic rocks. (a) Hand specimen of chlorite-talc schists. (b) Optical microphotographs (crossed nicols) showing the microstructure of foliated chlorite (Chl) schists that contain subhedral crystals of magnetite (Mag), ilmenite (Ilm) and apatite (Ap), seemingly in mineral equilibrium. The foliated microstructure defined by chlorite grain preferred orientations is unaffected or mildly deflected around apatite equidimensional grains. Some of the chlorite matrix grains exhibit undulose extinction. (c) Plane polarized light optical microphotograph of a large chlorite porphyrocrystal showing an intense replacement by ilmenite along its boundary and cleavage planes. (d) Scanning electron microscopy misorientation map showing the internal lattice organization of apatite grains (Ap, crystals shown with blue shades) embedded by a chlorite (Chl) matrix. Apatite microstructure is depicted by slightly strained domains with crystallographic orientations close to that of the average orientation of the host grain (rotated <3°, according to the colour scale bar at the right). Mineral abbreviations after Whitney and Evans (2010)

Pseudosections described by Padrón–Navarta et al. (2013) for the Cerro del Almirez (Spain) and Zermatt–Saas (Italy) serpentinites permit us to infer for mineral assemblages close to those studied here (containing chlorite and antigorite) $T < 490–450°$ under pressure 4–12 kb, and at $T < 450–410°$ under pressure <4 kb (most probable), that is, medium- to low-T greenschist facies conditions at pressure <0.4 GPa).

4.2 | Chlorite-talc schists

Chlorite-talc schists (Figures 9 and 10) are metamorphic rocks represented by sample 119 (Figure 3). They show a sparkling green colour in hand specimens (Figure 9a) and are dominated by chlorite in a modal proportion up to 98% (calculated after 93.27% successful EBSD indexation of the sample surface studied). The mineral assemblage in equilibrium includes chlorite, magnetite, ilmenite, apatite, talc and antigorite.

Chlorite occurs either in the fine-grained matrix with a shape-preferred orientation that defines a lepidoblastic microstructure (Figures 9b, d and 10a, b) or as porphyroclasts up to a few millimetre in grainsize (Figures 9c and 10c–e). In the latter case, chlorite deformation microstructures include microfolds, fan-like laminae detachments and recrystallized grains (Figures 10c–e). Matrix chlorite microstructures consist of bands with crystals showing a prominent shape-preferred orientation that isolates sub-millimetre bands with seemingly misoriented crystals (Figure 10b). Chlorite mineral chemistry corresponds to clinochlore (Figure 13) without significant compositional differences among the analyzed grains. Mineral formulae bear 5.65–6.05 Si atoms per formula unit (a.p.f.u., for O = 14) in the range for a constant $Fe^{3+}+Fe^{2+}$ content of ~1.0.

Finer-grained talc aggregates surround chlorite porphyroclasts and infill the open spaces created by its heterogeneous deformation, suggesting a late-stage growth (Figure 10c–e). In these aggregates, idiomorphic

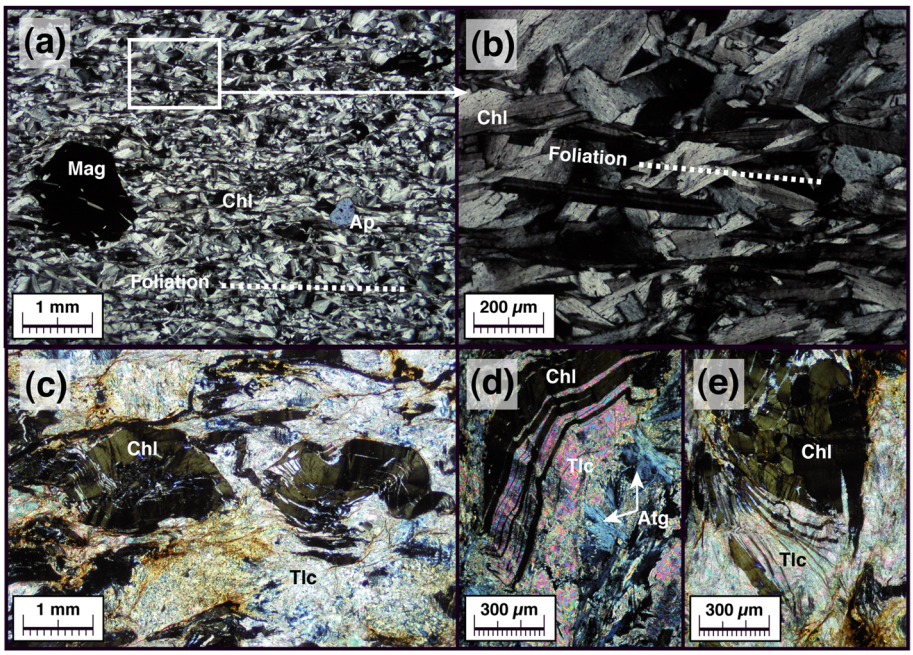

FIGURE 10 Optical microphotographs of chlorite-talc schists from mineralogically heterogeneous metamorphic ultramafic rocks. (a) Optical microphotographs (crossed nicols) showing the microstructure of foliated chlorite (Chl) schists that contain subhedral crystals of magnetite (Mag) and apatite (Ap). (b) Closer view of the white rectangle area in Figure 10a showing the arrangement of chlorite crystals in the matrix. It consists of bands with crystals showing a prominent shape-preferred orientation parallel to the foliation and of interleaved sub-millimetre bands with seemingly misoriented crystals. (c) Optical microphotograph under crossed nicols showing a refolded microstructure of chlorite porphyroclasts (Chl) embedded by a much finer grained talc-rich matrix (Tlc) in chlorite-talc schists. (d) Partially detached, very thin chlorite sheets (Chl) from a deformed porphyroclast in equilibrium with blade-like antigorite crystals (Atg) exhibit open spaces occupied by talc monocrystals (Tlc), the whole ensemble being subsequently microfolded (crossed nicols). (e) The microphotograph shows a microstructure in part similar to Figure 10d, but in this case, the core chlorite crystal (Chl) is composed of an aggregate of equidimensional recrystallized subgrains and new grains. Mineral abbreviations after Whitney and Evans (2010)

antigorite crystals may occur in textural equilibrium (Figure 10d). Talc may also appear in fibrous (antitaxial) veins together with carbonates and opaque minerals, crosscutting matrix microstructures. In some samples, talc may represent up to 20–30% in modal proportion.

These lithologies may also contain minor amounts of millimetre- to centimetre-sized idiomorphic magnetite, hematite, ilmenite (identified by XRD and indexed with EBSD) and apatite (also EBSD-indexed) in textural equilibrium with chlorite (Figure 9b and d). Opaque minerals may also occur along chlorite exfoliation planes/rims (Figure 9c). Magnetite can be a significant mineral component (<1%). Apatite (also <1% in modal proportion) occurs as subhedral crystals (<1 mm in their largest dimension). They can either curve slightly the neighbour matrix chlorite flakes (Figure 9b) or clearly postdate the microstructure of the matrix without deflection (Figures 9b and 10a). In sections perpendicular to the foliation and parallel to the lineation, they can be subparallel to the orientation of chlorite and exhibit aspect ratios up to 7. EBSD misorientation maps of these grains (Figure 9d) show that they are essentially monocrystals, with faint lattice distortions and domains rotated less than 2° with respect to their host. These characteristics are congruent with syn- to post-tectonic apatite growth. Mineral composition data of these phases are included in Table S2.

4.3 | Tremolite-talc ultramafic rocks

These rocks (represented by sample 134; Figure 3) show a greenish-grey colour in fresh exposures and exhibit an outstanding planolinear fabric (Figure 11a). Amphibole (up to 96% in modal proportion, calculated with optical methods because successful EBSD indexation of the sample surface studied was only 53.74%), chlorite (<2%) and talc (<2%) occur as the constituent phases of the mineral assemblage in equilibrium and define a nematoblastic microstructure (Figure 11b). XRD analyses pointed also to the presence of traces of a second, Fe-Mg monoclinic amphibole.

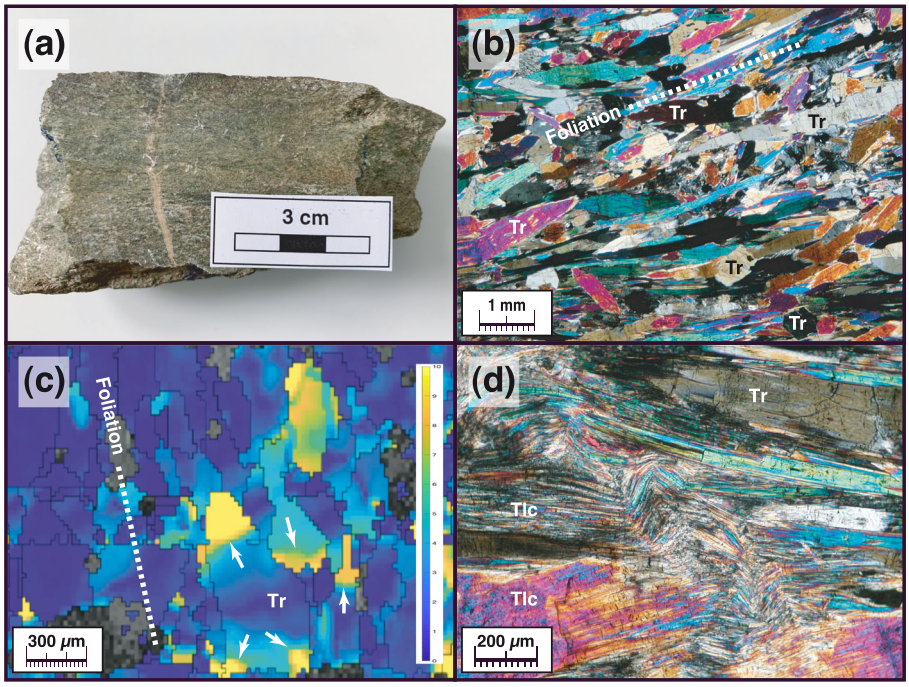

FIGURE 11 (a) Hand specimen of tremolite-talc-chlorite ultramafic rocks. (b) Optical microphotograph (crossed nicols) showing the strong shape-preferred orientation parallel to the macroscopic foliation, defined by elongate tremolite (Tr) crystals showing solid-state deformation microstructures such as undulose extinction, dislocation walls and subgrains. (c) Scanning electron microscopy misorientation map showing the internal lattice organization of tremolite grains. Crystals shown with yellow tones correspond to distorted domains with crystallographic orientations departed ~10° from that of the neighbouring (blue) domains (some of the boundaries are marked with white arrows). The colour scale bar shown at the right permits to unravel that tremolite crystal lattices do not exhibit homogeneous orientations but smooth continuous orientation variations. (d) Optical microphotograph (crossed nicols) of coarse grained talc (Tlc) domains developed around tremolite (Tr) showing that the former accommodated in preference the superimposed deformation (resulting in microfolding and gliding along talc cleavage planes). Mineral abbreviations after Whitney and Evans (2010)

Amphibole mineral chemistry denotes it is Ca and Mg rich (Figure 14) and corresponds to Mg-rich actinolite and tremolite (henceforth, tremolite s.l.; Leake et al., 1997; Hawthorne et al., 2012). Despite its limitations (originally proposed for epidote-bearing mafic schists containing quartz and albite), the Al^{IV}–Al^{VI} bivariate diagram of Laird and Albee (1981) shows that these metamorphic amphiboles plot in the field of the greenschist facies (Figure 15). Padrón–Navarta et al.'s (2013) pseudosections permit us to attain a similar conclusion for mineral assemblages close to those studied here (high-T greenschists to low-T amphibolite facies at pressure <0.4 GPa).

Tremolite exhibits columnar to acicular idiomorphic habits, crystal facets and the characteristic sets of cleavage planes in basal sections. In schistose lithologies, tremolite exhibits a strong shape-preferred orientation parallel to the foliation and lineation (Figure 11b). Crystals with large aspect ratios up to 15 and millimetre-scale longest dimensions exhibit a gentle exfoliation plane curvature that grades into undulose extinction and even leads to isolation of subgrains (Figure 11b–c). All these features point to crystal-plastic deformation mechanisms. EBSD misorientation maps (Figure 11c) reveal smooth to discrete tremolite lattice distortions and low angle grain boundaries. This microstructure points to rearrangement of dislocations along grain boundaries, leading to the eventual formation of new grains by crystal–plastic mechanisms.

Talc occurs in close association with tremolite and minor chlorite, and contributes to define the rock fabric (Figure 11d). Talc underwent heterogeneous deformation facilitated by the strong sheet anisotropy of the crystals (microfolding and kinking). The textural relationships with respect to tremolite suggest that talc replaced it synkinematically along grain boundaries, though both phases appear to form as well an equilibrium (or a metastable) assemblage.

Chlorite subhedral crystals (grain size <400 μm) occur in direct contact with tremolite and show a shape-preferred orientation parallel to the foliation. Large chlorite grains correspond to clinochlore (Si atoms per

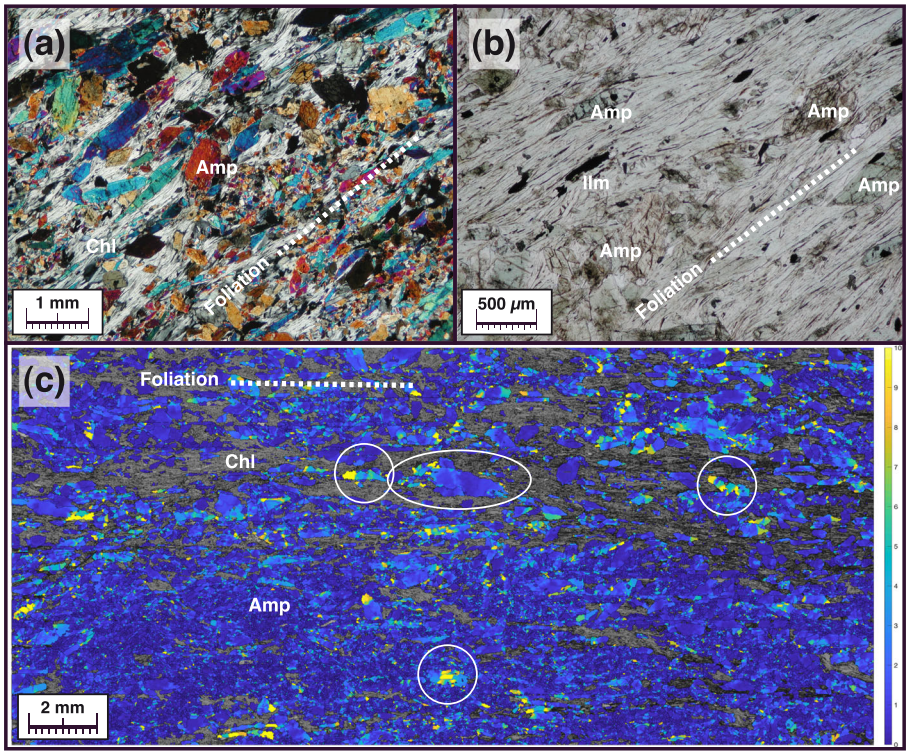

FIGURE 12 (a) Optical microphotograph (crossed nicols) of magnesio-hornblende-chlorite rocks showing that the rock fabric is defined by the shape-preferred orientation parallel to the macroscopic foliation of euhedral to elongate amphibole (Amp) and chlorite (Chl) crystals, sometimes with undulose extinction. (b) Closer view of the microstructure of chlorite-rich domains (plane polarized light). These localized deformation and gave rise to anastomosing foliations and shear bands at the microscale, isolating stretched amphibole crystals with congruent sigmoidal geometries. (c) Scanning electron microscopy misorientation map showing the internal lattice organization of amphibole grains. Crystals shown with yellow tones correspond to distorted domains with crystallographic orientations departed ~10° (recrystallized new grains, enclosed by the white circles) from that of the neighbouring (blue) domains. Amphibole crystal lattices do not exhibit homogeneous orientations, but smooth and discrete variations across boundaries oriented consistently oblique at a high angle to the foliation (e.g. the crystal enclosed by the white ellipse; see colour scale bar at the right for quantitative relationships). Mineral abbreviations after Whitney and Evans (2010)

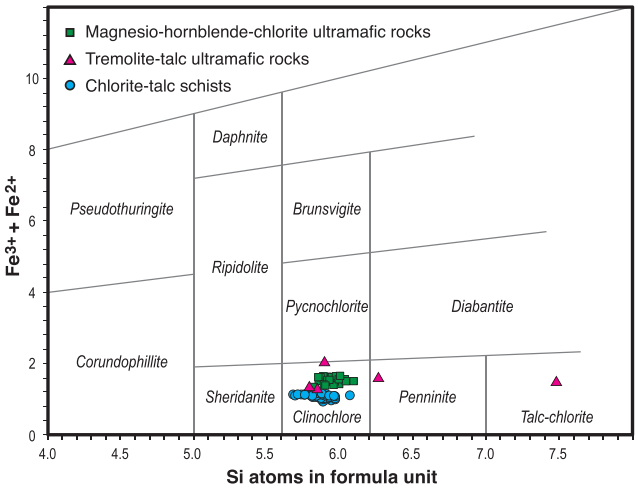

FIGURE 13 Chlorite compositions plotted in the diagram of Hey (1954)

formula unit in the range 5.30–5.70 for a $Fe^{3+} + Fe^{2+}$ content between ~1.2 and 2.0), whereas strained smaller grains (likely secondary) show penninite and talc-chlorite compositions (Figure 13 and Table S2).

4.4 | Magnesio-hornblende-chlorite ultramafic rocks

These rocks (represented by sample 124; Figure 3) correspond to chlorite-ultramafic rocks made of 70% hornblende and 29% chlorite (modal proportions calculated after 99.68% successful EBSD indexation). They are characterized by a bluish grey colour in fresh sections and by the development of a clear planolinear (nemato-lepidoblastic) fabric. The mineral assemblage in equilibrium, apart from amphibole and chlorite, includes ilmenite, apatite and zircon (jointly <1% in modal proportion).

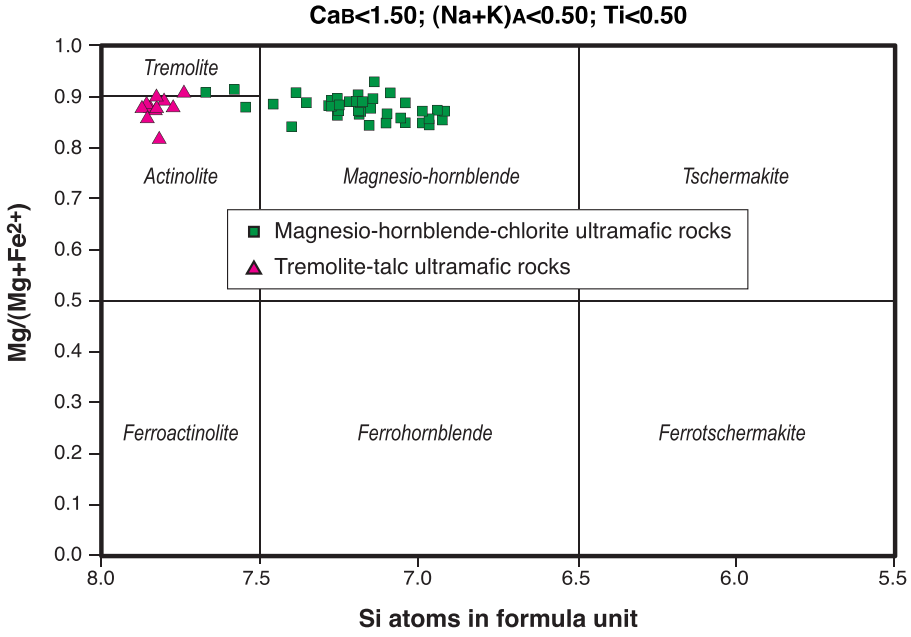

FIGURE 14 Amphibole compositions and classification according to the International Mineralogical Association (Leake et al., 1997) reference scheme

Amphibole is the framework-supporting mineral. Individual grains show longest dimensions up to 3 mm and exhibit a distinct shape-preferred orientation with aspect ratios up to 9 parallel to the foliation and the mineral lineation (Figure 12a and c). The most elongated crystals may exhibit undulose extinction (Figure 12a), consistently oblique dislocation tangles at a high angle to the foliation (area highlighted by ellipse in the Figure 12c), subgrain boundaries perpendicular to the elongation direction of the crystals (encircled areas in the Figure 12c) and microcracks normal to the lineation (Figure 12b), denoting stretching components parallel to it. Amphibole composition corresponds to magnesio-hornblende (Figure 14), although compositions transitional to tremolite and actinolite are also present. Projection of these mineral compositions in the Al^{IV}–Al^{VI} diagram of Laird and Albee (1981) places them in the metamorphic amphibolite facies domain, with minor data plotting in the epidote-amphibolite facies domain (Figure 15). This suggests that the metamorphic grade of these rocks and of their fabrics is distinctly higher than that of the tremolite-talc rocks. However, this observation may also relate to differences in the bulk rock Al content.

Chlorite crystal flakes contribute remarkably to the definition of the foliation (Figure 12a b). Geochemical analyses reveal a clinochlore mineral composition (Figure 13) with Si atoms per formula unit (for O = 14) in the range 5.80–6.08 and total Fe contents (Fe^{3+}/Fe^{2+}) between 1.32 and 1.60, calculated through charge balance criteria following Droop (1987). Individual crystals may reach up to 1.2 mm in their longest dimension and a few hundreds of micrometres across. Rock domains where chlorite modal proportion exceeds that of amphibole exhibit anastomosing foliations and shear bands at the microscale, isolating sigmoidal amphibole crystals (Figure 12b).

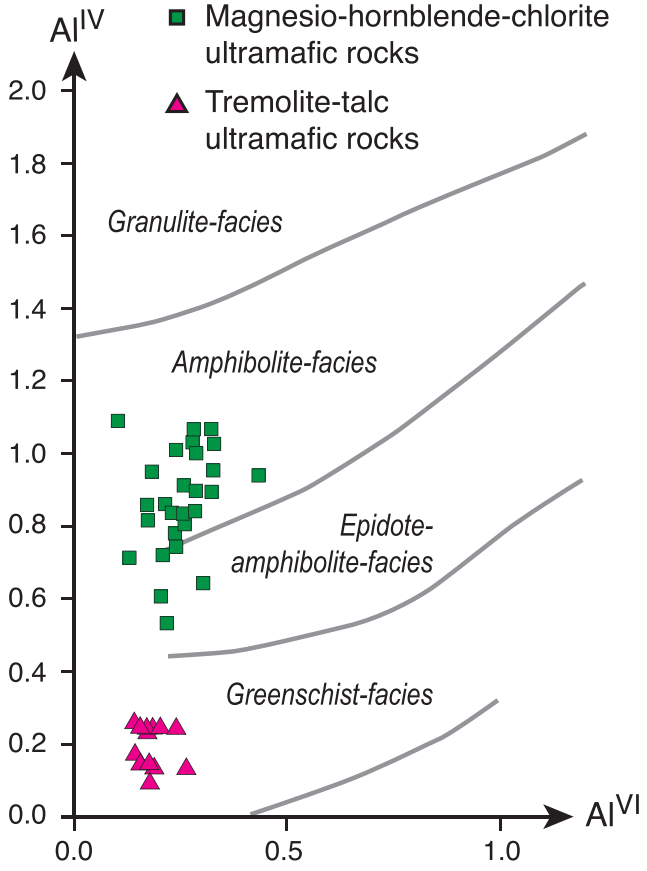

FIGURE 15 Plot of amphibole compositions in the Al^{IV}–Al^{VI} bivariate diagram of Laird and Albee (1981)

Apatite is occasionally present as small crystals with a maximum size of 200 μm and aspect ratios up to 2. No recognizable shape-preferred orientation can be observed. However, lattice misorientation maps show angular distortions inside grains of up to 7°. Opaque minerals show morphologies elongated parallel to the macroscopic foliation/lineation. Ilmenite is the most frequent opaque phase, with an Fe-rich composition of $Ilm_{90–93}$ and minor contents of pyrophanite (Mn component) and geikielite (Mg component). Mineral compositions of these phases are included in Table S2.

5 | PETROFABRIC

5.1 | Chlorite

Chlorite lattice-preferred orientation (LPO) patterns in the samples studied are similar (Figure 16), independent of the 98% modal proportion in chlorite-talc schists (Figure 16a), 1.5% in tremolite-talc rocks (Figure 16b) and 29% in magnesio-hornblende-chlorite rocks (Figure 16c). A significant texture intensity is supported by the respective Bunge's (1982) fabric texture indices (J) of 5.8, 9.3 and 5.4. LPO stereoplots show strong concentrations of the poles to chlorite (001) close to the Z structural direction with departures <15°. As regards the PGR texture indices (Vollmer, 1990), the poles to (001) planes exhibit the maximum values for the *P* (point maxima) index (0.28–0.61) and the correspondingly lowest values for the *R* (random) index. The [100], [010] and [110] axes exhibit spatial distributions close to girdles either with a faint ([100] orientations forming 5–10° with the *X* direction) or a slight (consistent) obliquity with respect to the foliation plane (<10–15° in the case of the [010] and [110] directions). Higher-density crystallographic axis concentrations within girdles track the

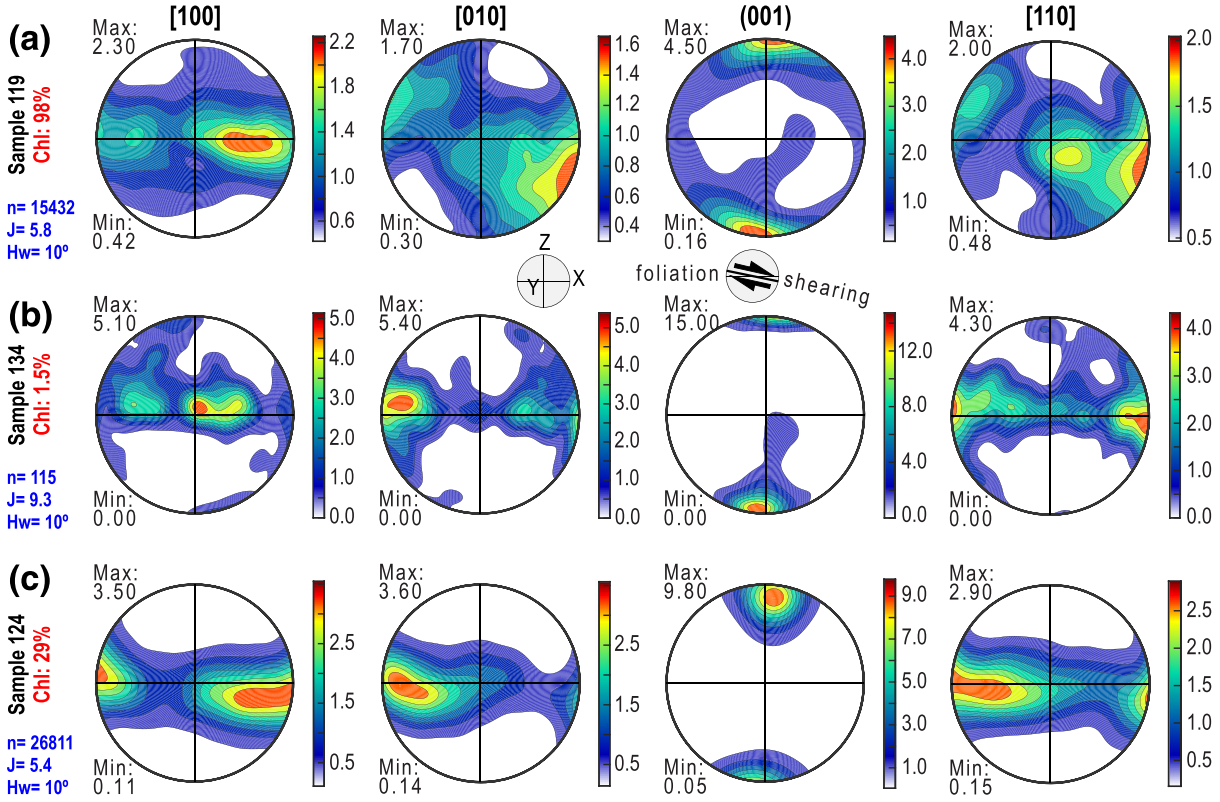

FIGURE 16 Chlorite LPO patterns from (a) chlorite-talc schists (sample 119), (b) tremolite-talc rocks (sample 134) and (c) magnesio-hornblende-chlorite rocks (sample 124). Stereogram colour patterns represent multiples of mean uniform density (specifically scaled in each lateral bar). Maximum and minimum concentrations are numerically expressed at the upper and lower left of each LPO, respectively. Lower hemisphere, equal area stereographic projections of XZ structural sections. Reference foliation is the equatorial diameter E-W, and the lineation is horizontal within that plane, as denoted by *X*, *Y* and *Z* in the small labelled circle between Figure 16a and b. The geometry of inferred rotational deformation components is depicted by the small circle with black half-arrows also placed between Figure 16a and b. J: Bunge's (1982) texture index; Hw: halfwidth value used for ODF (orientation distribution function) estimation; *n*: number of grains used to construct the diagrams. Mineral abbreviations after Whitney and Evans (2010), accompanied by their respective modal proportions in per cent

mineral/stretching lineation. These features reveal non-coaxial deformation components.

5.2 | Amphibole

LPO patterns for amphibole (Figure 17) show remarkable coincidences in spite of its different composition and modal proportion in tremolite-talc rocks (Figure 17a) and in magnesio-hornblende-chlorite rocks (Figure 17b).

Tremolite LPO (Figure 17a) shows a *J* texture index of 3.4. It depicts mixed girdle-point maxima distributions for the [001] directions and the poles to (100) and (110) planes. The point maxima within the girdles are concentrated close to *Z* in the case of the poles to (100) planes and around *X* ([001] for the poles to (110) planes. The highest *P* index values correspond to (100) planes (0.34) and [001] directions (0.33), which are within <10° close to the macroscopic foliation and <5° with respect to the mineral-stretching lineation, respectively. The orientation of the poles to (010) planes is not straightforward from the LPO, whereas that of (110) planes exhibits a close geometrical relationship of perpendicularity with respect to both the foliation and lineation.

Magnesio-hornblende LPOs (Figure 17b) are characterized by a smaller texture index ($J = 1.5$) than tremolite. They exhibit point maxima distributions within wide girdles for all the crystallographic elements measured, which are also aligned close to the principal macroscopic structural directions. It is remarkable the case of the poles to prismatic planes (100), (010) and (110), which define girdles normal to the lineation containing point maxima close to *Z*. The point maxima, however, associate low *P* index values, the largest one (0.14) corresponding to the distribution of the (010) planes. On its part, [001] crystal directions are preferentially concentrated in a girdle parallel to the macroscopic foliation with a point maximum parallel to *X*. This crystallographic direction exhibits the highest *G* (girdle) (0.41) and the lowest *R* (0.49) indices.

A very small but consistent obliquity is shown by the LPOs between girdles, point maxima and the *XYZ* reference framework. This supports the occurrence of non-coaxial deformation components during the amphibolite to epidote-amphibolite facies (magnesio-hornblende-chlorite rocks) and the greenschist facies (tremolite-talc rocks) P–T conditions prevalent during deformation of these rocks.

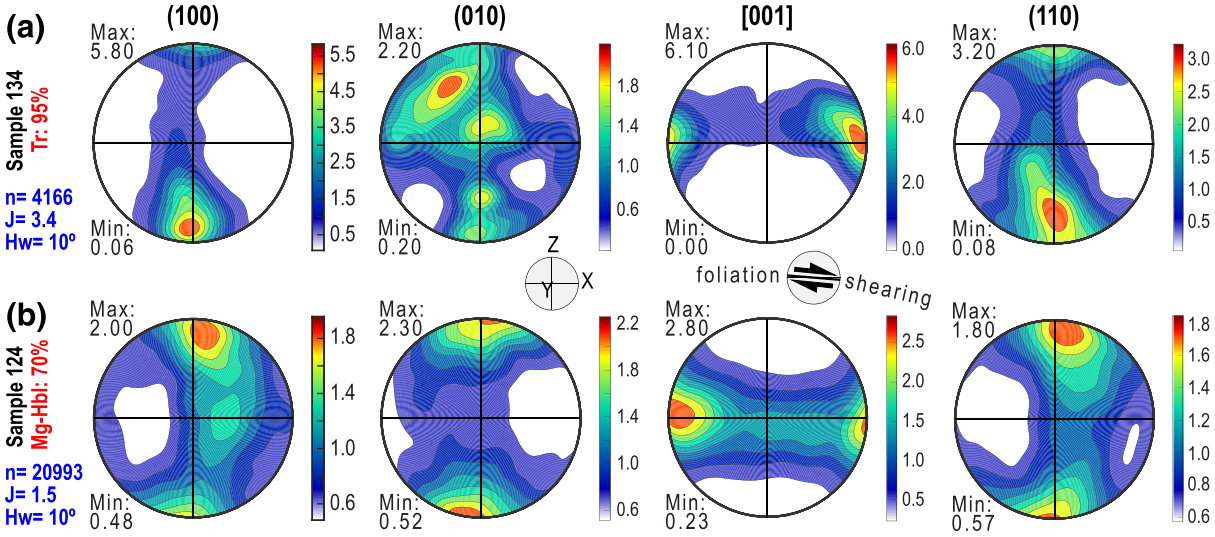

FIGURE 17 Amphibole LPO patterns of (a) tremolite from tremolite-talc rocks (sample 134) and (b) magnesio-hornblende from magnesio-hornblende-chlorite rocks (sample 124). Stereogram colour patterns represent multiples of mean uniform density (specifically scaled in each lateral bar). Maximum and minimum concentrations are numerically expressed at the upper and lower left of each LPO, respectively. Lower hemisphere, equal area stereographic projections of *XZ* structural sections. Reference foliation is the equatorial diameter E-W, and the lineation is horizontal within that plane, as denoted by *X*, *Y* and *Z* in the small labelled circle between Figure 17a and b. The geometry of inferred rotational deformation components is depicted by the small circle with black half-arrows also placed between Figure 17a and b. J: Bunge's (1982) texture index; Hw: halfwidth value used for ODF (orientation distribution function) estimation; *n*: number of grains used to construct the diagrams. Mineral abbreviations after Whitney and Evans (2010), accompanied by their respective modal proportions in per cent

5.3 | Talc, apatite and ilmenite

Talc LPOs from tremolite-talc rocks (Figure 18a) exhibit a very large texture index ($J = 25.2$). Among them, it is remarkable the distinct point maxima concentration of poles to the basal planes (001) at a very low angle (<5°) to the foliation normal. The obliquity sense with respect to the XYZ reference concurs with that shown by other minerals from the same sample and can be interpreted on the same grounds. Basal planes are the crystallographic element with the highest P (0.65) and the lowest R (0.10) indices. The [100] and [010] directions outline incomplete girdles along the foliation with point concentrations close to the X ([100] axes) and the Y ([010] axes) structural directions.

Apatite and ilmenite LPOs from magnesio-hornblende-chlorite rocks (Figure 18b–c) characterize the fabric of accessory minerals. Although the number of detected grains was relatively small ($n = 132$ apatite and 580 ilmenite grains), the LPOs are significant (J texture index values of 2.4 and 2.2, respectively). The LPO pattern of apatite (Figure 18b) includes [0001] axes concentrations within a wide girdle along the foliation plane, bearing high-density point concentrations in the vicinity of X. By contrast, the poles to {11–20} and {10–10} plane sets outline poorly defined girdles with multiple point maxima, arranged nearly perpendicular to the lineation orientation, with a higher pole concentration around Z. The highest P value (0.25) corresponds to the poles of (10–10) planes. Ilmenite shows LPOs characterized by a strong point maxima concentration of [0001] axes perpendicular to the foliation (Figure 18c). The <11–20> and <10–10> directions exhibit wide girdle distributions roughly parallel to the XY plane. In the respective LPOs, isolated submaxima can be observed close to the lineation.

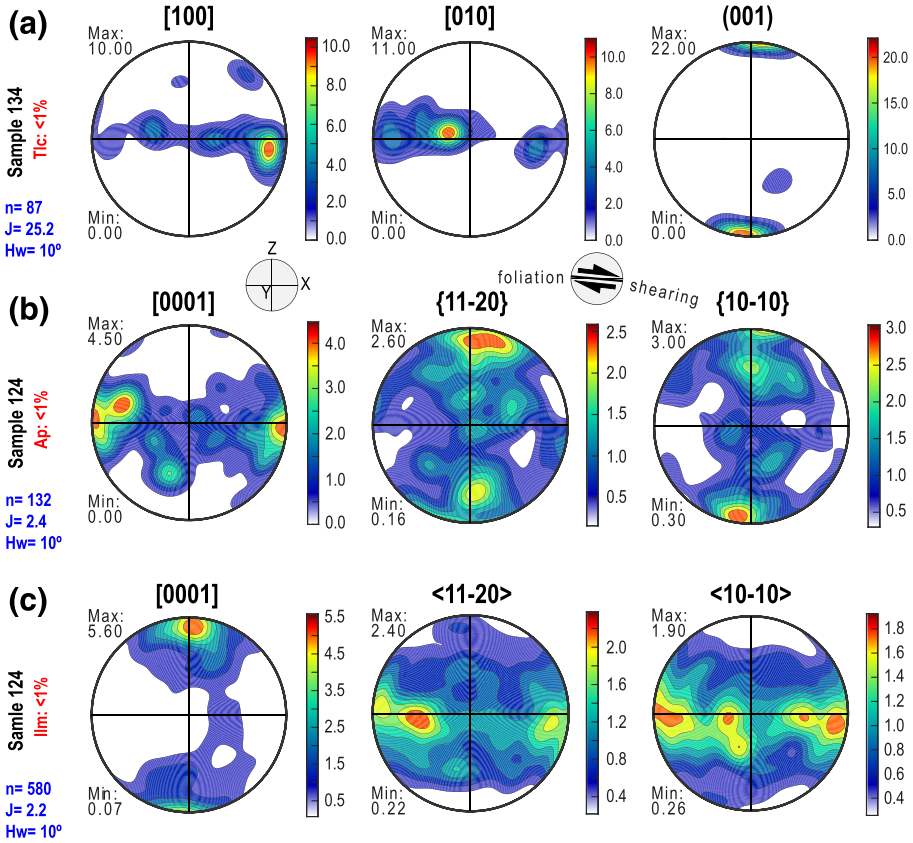

FIGURE 18 LPO patterns of (a) talc, (b) apatite and (c) ilmenite from tremolite-talc rocks (a; sample 134) and magnesio-hornblende-chlorite rocks (b and c; sample 124). Stereogram colour patterns represent multiples of mean uniform density (specifically scaled in each lateral bar). Maximum and minimum concentrations are numerically expressed at the upper and lower left of each LPO, respectively. Lower hemisphere, equal area stereographic projections of XZ structural sections. Reference foliation is the equatorial diameter E-W, and the lineation is horizontal within that plane, as denoted by X, Y and Z in the small labelled circle between Figure 18a and b. The geometry of inferred rotational deformation components is depicted by the small circle with black half-arrows also placed between Figure 18a and b. J: Bunge's (1982) texture index; Hw: halfwidth value used for ODF (orientation distribution function) estimation; n: number of grains used to construct the diagrams. Mineral abbreviations after Whitney and Evans (2010), accompanied by their respective modal proportions in per cent

A very small but consistent obliquity is shown by the talc, apatite and ilmenite LPOs and the *XYZ* reference framework. It is congruent with the obliquity determined after other mineral phases.

6 | APATITE U–PB AGES

One hundred and sixty valid analyses were selected from one hundred and sixty-one spot measurements performed in three thin sections from chlorite-talc schists (supplementary file Table S3), after rejection of results with error values higher >10%. Apatite U and Pb contents are always below 19.9 μg/g (average 6.1) and 12.3 μg/g (average 5.1), respectively, with $^{207}Pb/^{206}Pb$ ratios ranging from 0.31 to 2.12.

U–Pb results were processed online using IsoplotR (Vermeesch, 2018). Plotting of isotopic ratio data in Wetherill's concordia diagram (Figure 19a) shows that they are discordant, with upper and lower intercepts of 3738.9 ± 2.9 and 342.8 ± 12.2 Ma (MSWD = 1.4). If these discordant data are reported in the Tera–Wasserburg diagram (Figure 19b), an upper $^{207}Pb/^{206}Pb$ intercept of 0.3803 ± 0.0015 results. This was used to anchor an isochron that yields a lower intercept age of 342.8 ± 12.2 Ma (ages provided with 2σ errors, MSWD = 1.4).

7 | DISCUSSION

Ultramafic fragments similar to those studied here occur as dismembered sheets (tectonic slices) in metamorphic terranes of Phanerozoic continental domains worldwide. These were usually formed by metasomatism of ultramafic rocks during their regional metamorphic evolution in diverse tectonic settings. Then they were incorporated to the internal zones of orogens (where exhibit close relationships with HP metamorphic rocks). Petrographic observations and geochemical data from specific active tectonic settings provide evidence of a close relationship between chlorite-talc-tremolite rocks and serpentinized ultramafic protoliths. Among them, mid-ocean ridges (Escartín et al., 2003) and forearcs (Wang et al., 2009) are the most common, and oceanic core complexes, ocean-to-continent transitions, continental strike-slip faults and subduction channels are also possible (Guillot et al., 2015; Reynard et al., 1989; Wakabayashi, 2017). Serpentinite outcrops are surrounded there by sheared metasomatic irregular domains containing the aforementioned rocks, the origin of which is associated to Si metasomatism of serpentinite (Boschi et al., 2006; Nagaya et al., 2020). This proposal is supported as well by several studies of serpentinized ophiolites currently inserted in continental settings (Frost & Beard, 2007; Kang & Jung, 2019; Moore & Rymer, 2007). Below we discuss the results of this study from diverse perspectives that include the characteristics of serpentinization/metasomatism, the interpretation of rock petrofabrics, the likely tectonic context and the regional implications for the Cadomian geology of southwestern Europe.

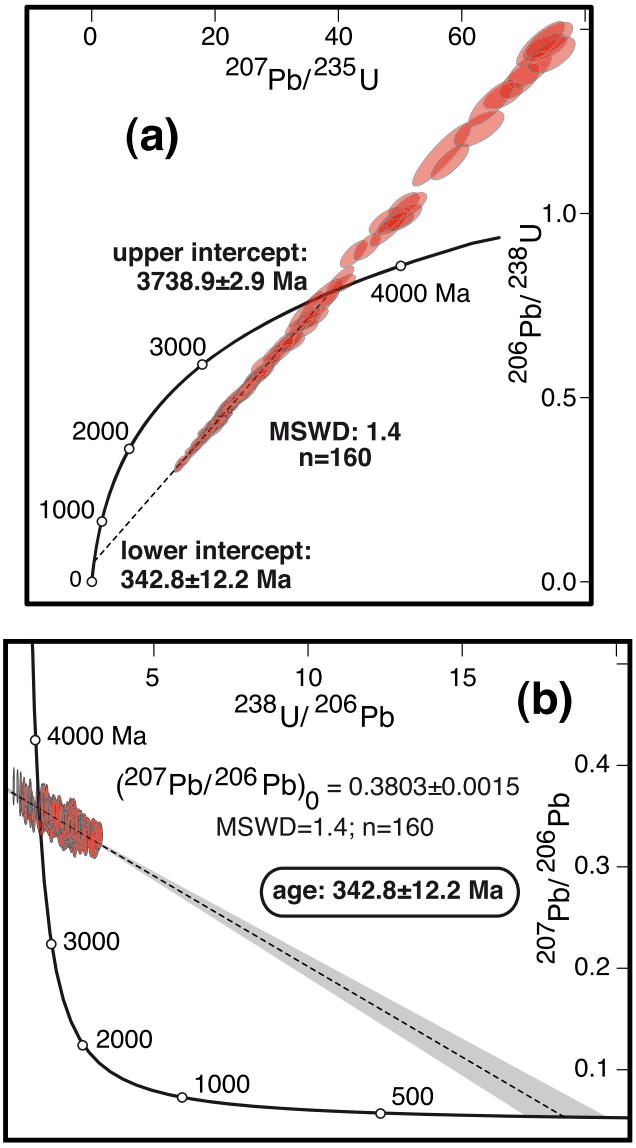

FIGURE 19 (a) Plot in the Wetherill's concordia diagram of $^{206}Pb/^{238}U$ vs. $^{207}Pb/^{235}U$ isotopic ratios from 160 apatite spots. (b) Plot in the Tera–Wasserburg's diagram of $^{207}Pb/^{206}Pb$ vs. $^{238}U/^{206}Pb$ isotopic ratios from the same apatite spots

7.1 | Serpentinization and metasomatism

The serpentinization of peridotite by water addition involves specific mineral reactions that affect the primary

olivine-orthopyroxene-clinopyroxene-spinel assemblage (Evans, 1977, 2004; Evans et al., 2013; Iyer, 2007; Wicks & Whittaker, 1977). These may produce serpentine directly after olivine, orthopyroxene and spinel, together with other alteration minerals (magnetite, brucite, chlorite and talc), and release various by-products in aqueous solution (SiO_2, H^+, Al^{3+} and O^{2-}) that can subsequently react with the primary assemblage or with their reaction products to generate second and third generation serpentine, magnetite, chlorite and talc (Iyer, 2007; Wang et al., 2009). Olivine alteration at $T < 400°C$ yields serpentine (lizardite; Boudier et al., 2010), brucite and magnetite. Spinel alteration results in the formation of magnetite, serpentine and chlorite (the latter forming aureoles) and releases the Al^{3+} needed to form additional chlorite after serpentine. Orthopyroxene hydration and metasomatic reactions yield either serpentine or talc + olivine (the latter mineral being replaced by serpentine if aqueous fluids are available).

Petrographic observations and mineral chemistry of the ultramafic rocks studied reveal a complex geological evolution during which the ultramafic precursors were totally serpentinized. The primary spinel facies, amphibole-bearing peridotite protoliths are here considered to be associated to a mantle wedge realm related to a plate convergence tectonic setting. This is supported by the nature and distribution of latest Ediacaran–earliest Cambrian magmatism in the area (Sarrionandia et al., 2020, and references therein). In principle, a fore-arc mantle wedge realm would be more likely, because refertilized peridotites from (back-arc) ocean–continent transitions are usually plagioclase bearing (Rampone et al., 1993). Fore-arc low PT serpentinization would have been driven by a plumbing system involving slab fluids.

The microstructure of the Type 1 foliated serpentinites (with penetrative fabrics, ghost SC microstructures, asymmetric porphyroclast systems and quarter structures with antigorite crystals in the shortening domains; Figure 4a–c) tracks non-coaxial ductile deformations. Petrographically, a primary serpentinization stage yielded lizardite and magnetite. Identification of antigorite bundles and blade-like crystals in sigmoidal porphyroclast systems and along the foliation point to a superimposed prograde syn-tectonic metamorphic overprint under higher P (>0.7 GPa) and T (>390°C; cf. Auzende et al., 2006; Guillot et al., 2015), rather than to a high-T origin for this mineral during primary serpentinization (e.g. Boudier et al., 2010; Reynard, 2013).

Type 2 serpentinites (Figure 5a–b) contain additional minerals in veins and secondary infillings (chrysotile, dolomite, talc and opaques) compatible with either low temperature primary alterations or with late retrogressions. The occurrence of oriented antigorite in the foliated matrix, however, suggests that these rocks experienced a metamorphic overprint with characteristics similar to those described for the Type 1 serpentinites. In this context, veins and their infillings might even be syn- to late-tectonic features, the chrysotile being the only clear post-tectonic mineral phase.

In the type 3 serpentinites with amphibole crystal pseudomorphs (Figures 6 and 7), the lizardite mesh microstructures disclose the primary low-pressure (<1.0 GPa) and low-temperature serpentinization (0–300°C; cf. Guillot et al., 2015) of an already metasomatized ultramafic rock containing idiomorphic amphibole crystals. The presence of those amphiboles might be ascribed to early metasomatic alterations after clinopyroxene at temperatures <800°C (Iyer, 2007). Alteration of this assemblage resulted in a fine-grained lizardite matrix with magnetite disseminations and in euhedral amphiboles fully altered as well by lizardite with a mesh microstructure. The lizardite matrix lacks a significant fabric but is postdated by tiny antigorite crystals with a preferred orientation (Figure 8a, b). These features point to a metamorphic overprint similar to that inferred for the other serpentinite types.

The close spatial association of Types 1–3 serpentinites with major thrust contacts and HP rocks (i.e. between para-autochthonous low-grade metapelites and allochthonous gneisses and retro-eclogites; Figure 3) supports the interpretation that antigorite foliation formed in relation with those structures. Also, because they are postdated by early Ordovician intrusives (section 2.1) and can reasonably be ascribed to the Cadomian D1 tectono-metamorphic evolution, antigorite growth might be related to prograde reworking during D1, which in the neighbouring units recorded HP metamorphic conditions.

The formation of the other mineralogically more heterogeneous metamorphic ultramafic rocks (chlorite-talc schists, tremolite-talc-chlorite rocks and magnesio-hornblende-chlorite rocks) required involvement of metasomatic agents. Even supposing that formation of chlorite (clinochlore) after spinel can be triggered by H_2O addition, its actual modal proportion would not be significant and would be in conflict with the observation that some rocks are composed almost completely by chlorite. Thus, chlorite rather was formed after abundant peridotite olivine, triggered by external addition of Al^{3+} (Iyer, 2007). In the case of talc, it can form after orthopyroxene and H_2O. However, olivine would be a product phase and no petrographic evidence supporting it was found. Alternatively, silica metasomatism of serpentine can result in significant modal proportions of talc, as observed in the samples studied. Metasomatic replacement of serpentine by talc involves Mg, Fe and Si mass transfer (SiO_2 should

be sourced externally) constrained by the reaction serpentine + $2SiO_2$ = talc + H_2O, a prograde reaction taking place at 300–450°C (Evans, 1977). Metasomatic alteration of precursory serpentinites can also explain the observed coexistence of chlorite and talc in equilibrium, because the latter phases do not result one from the other. Their microstructure suggests that chlorite crystallized earlier, and that both minerals were subsequently deformed. A tectonothermal overprint such as that inferred for the serpentinites would have not modified the equilibrium mineral assemblage of chlorite-talc schists. In fact, the occurrence of antigorite in textural equilibrium with talc and chlorite (Figure 10d) might support that the metasomatism was pre- to syn-metamorphic/tectonic.

Regarding the case of calcic amphibole-bearing assemblages, their occurrence can result from the combined hydration of primary orthopyroxene and clinopyroxene at *T* between 825 and 400°C. In well-studied cases, tremolite crystals commonly obliterate and hinder primary textures and mineral parageneses (Boschi et al., 2006). The hydrothermal alteration of mafic rocks (gabbro) under greenschist facies conditions produces amphibole and chlorite pseudomorphs after pyroxene and transforms them into amphibole schists releasing silica (which can promote metasomatism and talc formation in neighbouring serpentinites; cf. Iyer, 2007). Calcic amphibole serpentinization can take place at *T* below 480°C by involvement of H^+- and Fe^{2+}-bearing aqueous fluids, then releasing silica and Ca^{2+} solutes (Wang et al., 2009). In our samples, the close association of oriented chlorite, talc and tremolite aggregates, their mutual textural relationships, and their outstanding fabric suggest that they grew syn-tectonically, they were plastically deformed, and that talc was a relatively later phase. Tremolite mineral chemistry supports this occurrence under greenschist facies ambient *T* conditions. In principle, these characteristics might be ascribed to metasomatic/metamorphic transformation of a serpentinite precursor.

The ascription of the metamorphic overprint inferred above (postdating the primary serpentinization) to a Cadomian (D1) tectono-metamorphic evolution is based upon structural field criteria (major thrust contacts and penetrative deformations in HP rocks postdated by early Ordovician intrusives). It is, however, at odds with the 342.8 ± 12.2 Ma discordant isochron age from the apatite population from chlorite-talc schists. Apatite exhibits textural equilibrium with chlorite, talc and tremolite in chlorite schists and Magnesio-hornblende-chlorite rocks, where a syn-tectonic relationship with development of shape fabrics and LPOs of the other minerals can be inferred. Field relationships show also that a Variscan tectonothermal shear zone overprint affected with variable intensities all the rocks of the Badajoz–Córdoba belt. Likely, a strong overprint should be the expected case for mechanically weak serpentinite and related ultramafic rocks as the ones studied. Apatite U–Pb analyses have been used to date magmatic and hydrothermal events (e.g. Bouzari et al., 2016; Corfu & Stone, 1998), as well as exhumation and thermal overprints in metamorphic terranes (Hall et al., 2018; Krestianinov et al., 2021), even though its closure temperature ranges from 375 to 550°C (Cochrane et al., 2014; Harlov et al., 2005; Kirkland et al., 2018). In the Badajoz–Córdoba shear zone, a late Palaeozoic (Variscan) overprint under amphibolite to greenschist facies conditions has been robustly established and radiometrically dated by several authors (Figure 20 and references therein). Thus, the 342.8 ± 12.2 Ma apatite age might be related to such tectonothermal reworking and disconnected from the antecedent serpentinization, metasomatism and D1 metamorphism. Decoupling between isotopic systems used for radiometric dating (even of different systems in the same dated mineral; e.g. Beranoaguirre et al., 2019), trace elements, mineral chemistry and microstructures is being increasingly found when distinct stages of deformation-enhanced recrystallization are involved in metamorphic rock systems under an ample range of *P* and *T* conditions (Gordon et al., 2021).

7.2 | Interpretation of rock petrofabrics

The samples studied exhibit mineral assemblages in equilibrium depicted by crystals with conspicuous shape and LPO patterns. The corresponding microstructures evidence intracrystalline deformation and deformation accommodation by dislocation creep, possibly assisted by complementary mechanisms.

Equivalent chlorite LPOs are present in all the samples studied, independent of their modal proportion (from 2% to 98%). They correspond to the Type 1 of Kim and Jung (2015), characterized by (001) planes parallel to the foliation (with [100] and [010] axes contained in this plane). This LPO is well known in natural phyllosilicates (e.g. Kang & Jung, 2019; Puelles et al., 2012), as well as in experimental studies that show (001) planes usually acting as slip planes and [hk0] axes as dominant slip directions (Bons, 1988). The simple shear experiments of Kim et al. (2020) with chlorite peridotite starting materials suggest that Kim and Jung's (2015) Type-1 LPOs relate to low shear strains ($\gamma \leq 3.1$).

Tremolite LPOs fit Ko and Jung's (2015) Type I fabrics, which can be explained by activation of the intracrystalline slip system that involves (100) planes and

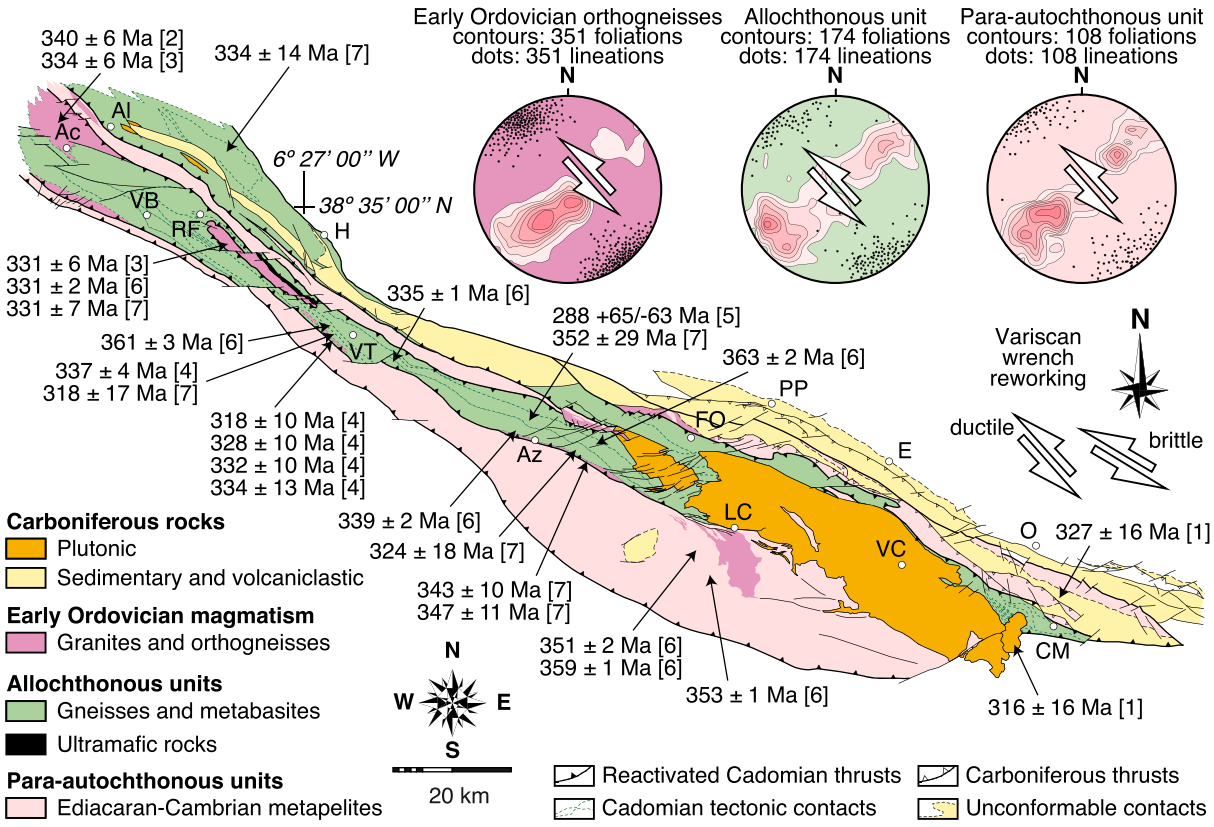

FIGURE 20 Geological sketch map of the Badajoz–Córdoba ductile shear zone including the sites that provided Variscan reworking metamorphic ages. Outcrops of a discontinuous tertiary cover have been removed in order to highlight the distribution of concealed geological units. See text for further details. Geochronological references: [1] Bellon et al. (1979); [2] Abranches et al. (1979); [3] Blatrix and Burg (1981); [4] García-Casquero et al. (1988); [5] Schäfer (1990); [6] Quesada and Dallmeyer (1994); [7] Ordóñez-Casado (1998); [8] this study. Localities: Ac, Aceuchal; Az, Azuaga; Al, Almendralejo; CM, Cerro Muriano; E, Espiel; FO, Fuente Obejuna; H, Hornachos; LC, La Cardenchosa; O, Obejo; PP, Peñarroya-Pueblonuevo; RF, Ribera del Fresno; VB, Villafranca de los Barros; VC, Villaviciosa de Córdoba; VT, Valencia de las Torres

[001] axes as flow planes and directions, respectively. It is well-known in both natural and experimental amphibole deformation studies (e.g. Dollinger & Blacic, 1975; Rooney et al., 1975) and constitutes the least resistant glide surface following the weak interchain bounds between Ca/Mg and O in the crystal framework (Baratoux et al., 2005; Cumbest et al., 1989; Rooney & Riecker, 1969; Skrotzki, 1992). For this reason, this fabric type is usually found in amphiboles deformed from low to intermediate temperatures (up to those of the amphibolite facies) under varied stress conditions. Magnesiohornblende LPOs compare to those of tremolite, but, in this case, the occurrence of a point maxima distribution for the poles to (010) planes (in addition to [100] poles) normal to the foliation can be taken as an indicator of cooperative action of (100)[001] and (hk0)[001] slip systems (Zhang et al., 2013), under temperatures <650°C and low stress conditions (Biermann & Van Roermund, 1983; Puelles et al., 2016; Reynard et al., 1989; Rooney et al., 1975; Skrotzki, 1992). The distinct equilibrium conditions determined for these minerals after their mineral chemistry (Figure 15) and activation of the (hk0)[001] slip system in magnesiohornblende are the clues to interpret that deformation of tremolite-bearing rocks occurred under lower temperatures, characteristic of the greenschist facies. Other amphibole deformation mechanisms such as twinning, rigid body rotation, dissolution–precipitation or oriented growth might have played a complementary though minor role during the process of strain accommodation, attending to the absence of diagnostic microstructural features.

Talc microstructures and LPOs concur with the results of previous studies (e.g. Nagaya et al., 2020) that highlight deformation of this mineral is accommodated at all temperatures by crystal plasticity, frictional sliding and cataclasis (Escartín et al., 2008). Kinking and bending microstructures are common in the rocks studied, facilitated by easy slip along basal planes (Morrow et al., 2000). The LPOs suggest operation of the (001)

[100] intracrystalline slip system widely reported for the case of deformation studies on phyllosilicates (see above). Though it has been rarely studied so far with the EBSD technique, the fabric of talc in mafic/ultramafic schists and related rocks (Nagaya et al., 2020) presents several characteristics similar to that of antigorite (Soda & Wenk, 2014; Van De Moortèle et al., 2010), as well as a comparable seismic response and anisotropy (Bezacier et al., 2010; Jung, 2011; Katayama et al., 2009; Nishii et al., 2011). For this reason, the presence of talc rocks in subduction zones and continental sutures is thought to contribute to sliding in the subduction zone slab mantle interface and in seismically active faults (Hirauchi et al., 2010; Ji et al., 2013).

Apatite shape-preferred orientation and LPOs can be explained, in principle, by preferential growth along the [0001] direction (Nakano et al., 2001). However, evidence of crystal distortion (intragrain lattice misorientations across discrete boundaries) points to components of deformation accommodation by crystal–plastic mechanisms (Ribeiro et al., 2020) that involved activation of the {10–10}[0001] intracrystalline slip system (Nakano et al., 2001; Saka et al., 2008).

Possible relationships with deformation of the ilmenite LPOs reported in this study are compatible with the activation of the (0001) < 11–20 > intracrystalline slip system. Current knowledge of ilmenite plastic deformation mechanisms is meagre. However, the same slip systems might be expected to operate as in the isostructurally equivalent corundum (Barber et al., 2010).

The small but consistent obliquity between LPOs and the XYZ reference framework depicted by all the minerals studied (chlorite, tremolite, magnesio-hornblende, talc, apatite and ilmenite) points to non-coaxial deformation components during solid-state deformation of these rocks. Those components are congruent with their metamorphic characteristics and their structural context, sandwiched between two major metamorphic thrust slices.

7.3 | Tectonic context

Serpentinites are intimately associated to HP metamorphic rocks in suture zones of a varied geographical and chronological range, linking them to paleosubduction zones (Guillot et al., 2015). They are regarded as fragments of oceanic lithosphere first subducted and then exhumed by a combination of return flow and buoyancy forces. Release of fluids along portions of the subducting slab (Hyndman & Peacock, 2003) increases the serpentinization of the mantle wedge (30–100%), which is thought to result in up to 2–3 km thick layers of strongly foliated serpentinite in subduction channels, potentially stable to depths below 120 km. Tectonic decoupling between the stagnant mantle wedge and the subducting plate would be accommodated by a weak serpentinite layer (a few hundreds of metres thick) concentrating deformation and large displacements in shear zones centimetre to hectometre thick. The process leads to generalized foliation development, syn-tectonic crystal growth, and to a plastic mechanical behaviour (Amiguet et al., 2014). Talc produced by a high silica activity during serpentinization or by serpentinite dehydration during prograde metamorphism dramatically weakens those shear zones (Kohli et al., 2011). Subducted sediment abundance can contribute as well to soften further the plate interface through hydration of the mantle wedge and tectonic mélange development after fragments of both the overriding and the subducted plates. This tectonic scenario also plays a major role in the exhumation of neighbour HP rocks, which include kilometric eclogitic blocks exhumed from depths of about 70–80 km (Agard et al., 2009; Guillot et al., 2009). Taking all the above into account, serpentinite units from HP settings may contain serpentine tectonites and talc- and/or chlorite-bearing ultramafic rocks, in addition to metamorphic blocks of different sizes and origins. The latter are usually dispersed in a strongly sheared matrix and record contrasting *P*–*T* conditions (Angiboust et al., 2011). This scenario compares to the units studied herein and would share similar petrofabrics and seismic geophysical properties (Hirauchi et al., 2010; Jung, 2011; Nishii et al., 2011).

A current equivalent scenario from a subduction setting might be the Mariana forearc in the southern Izu–Bonin–Mariana lithosphere convergence system (Figure 21). There, serpentinite (Wang et al., 2009) and HP metamorphic clasts (blueschists; Tamblyn et al., 2019; Ichiyama et al., 2021) currently exposed in the landward slopes of the trench have been exhumed to the seafloor from the mantle wedge. Serpentinized peridotite samples dredged contain the olivine-spinel-amphibole mineral association. Amphiboles are Ca-rich tremolite and magnesio-hornblende, exhibit columnar or needle-shaped idiomorphic habits, crosscut (postdate) the serpentine mesh texture, and are usually also serpentinized. Chlorite and talc replacing serpentine or forming veins are also present. All this fits closely to the characteristics of the ultramafic rock assemblage described in this study. Guillot et al. (2009, and references therein) suggest that tectonic associations such as those described are often related to magmatic arcs, advocating for prior warm subduction. This might also be the case for the area studied here (Sarrionandia et al., 2020).

The Mariana forearc exhibits additional features that can be correlated to the Cadomian tectonic organization

of the OMZ. The magmatic arc is constructed on oceanic to transitional crust and is split from S to N into two branches separated by the Mariana trough, which is an active back-arc basin floored by oceanic lithosphere (Figure 21a). The OMZ counterpart shows two magmatic arc segments as well. These currently expose volcanic and plutonic rocks in the surface separated by a metamorphic belt that contains HP rocks (the Badajoz–Córdoba shear belt; Figure 21b). The two magmatic arc branches and the intervening metamorphic belt are intimately related to the Ediacaran Serie Negra, which extends across the area and represents a volcano-sedimentary basin infill. Some parts of it occupy southern positions in current coordinates that concur with a fore-arc tectonic setting (Rojo-Pérez et al., 2019). In those realms, Akker et al. (2020) have described and dated blueschist facies rocks older than 550 Ma. Other Serie Negra areas to the N, for their part, concur with intra-arc to back-arc environments (Rojo-Pérez et al., 2021). Further N, coeval sedimentary successions record a distinct back-arc imprint and the OMZ Serie Negra realm would have been accreted to it by the latest Ediacaran, as the Palaeozoic sequences on top of both record an identical provenance (López-Guijarro et al., 2008).

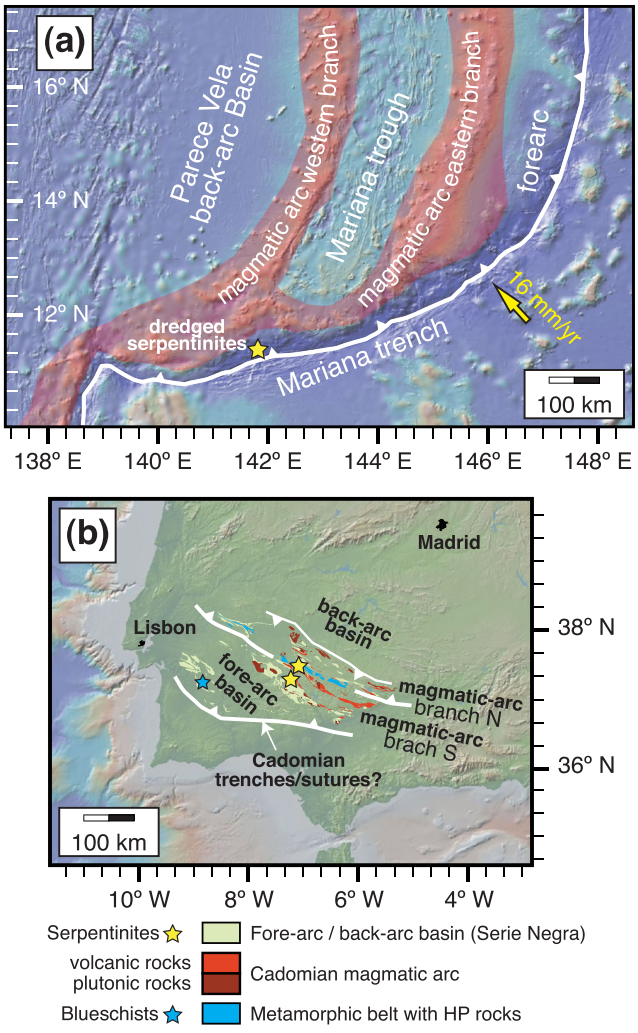

FIGURE 21 Solid earth surface topography of the (a) southern Izu–Bonin–Mariana arc system and of the (b) SW Iberian Peninsula presented at the same scale for comparison after GeoMapApp data (Ryan et al., 2009). Figure 21a shows the areal distribution of the subduction trench (white lines) and the associated magmatic arc (transparent red overlay), split by the Mariana trough active back-arc basin (floored by oceanic lithosphere). The yellow star shows the site where talc-tremolite-chlorite and other serpentinized ultramafic rocks similar to those studied here were dredged (Wang et al., 2009). (b) Distribution of late Ediacaran–earliest Cambrian magmatic rocks associated to Cadomian subduction (Sarrionandia et al., 2020), of partly coeval arc-related volcano-sedimentary successions (the Serie Negra), and of the HP metamorphic belt. Yellow stars: serpentinite occurrences. Blue star: >550 Ma blueschists (Akker et al., 2020). Current width and separation of these belts resulted from poly-orogenic arc shortening and wrench displacements

7.4 | Regional geological implications

Evidence of Cadomian lithospheric convergence in SW Iberia (active from c. 750 Ma up to c. 540 Ma; Linnemann et al., 2014) is supported by arc magmatism (Bandrés et al., 2002, 2004; Sarrionandia et al., 2020) and subduction-related metamorphic rocks (Ábalos et al., 1991; Akker et al., 2020). Subsequent reworking included intracontinental magmatism related to crustal-scale rifting (Cambrian–early Ordovician; Sánchez-García et al., 2008) and late Palaeozoic wrench tectonism (Eguíluz et al., 2000).

Formation of juvenile crust in the Cadomian magmatic arc involved melt extraction from asthenospheric and heterogeneously enriched mantle sources (Bandrés et al., 2004; Sánchez-Lorda et al., 2016). It has been usually related to an arc setting constructed on a c. 2 Ga old transitional crust (Linnemann et al., 2014), because the oldest arc-rocks from the OMZ lack a significant continental crust signature (e.g. López-Guijarro et al., 2008; Pin et al., 2002). The latest stages of the evolution of the Cadomian arc (c. 534 Ma ago) record crustal growth after reworking/melting of basic-ultrabasic, thin crustal and mantle-derived rocks (Sarrionandia et al., 2020). The serpentinized and metasomatized ultramafic rocks studied herein would represent supra-subduction arc mantle fragments accreted to such an arc in a structural context different from that proposed for the Calzadilla ophiolite counterpart (Díez Fernández et al., 2019). The Ribera del Fresno–Llera ophiolite is sandwiched between two major metamorphic thrust units that record a HP metamorphic imprint. It was also affected by a relatively HP

metamorphism that postdates previous stages of low-temperature and low-pressure serpentinization and metasomatism. The resultant metamorphic belt, likely representing a subduction channel, currently separates two parallel Cadomian arc segments containing plutonic and volcanic rock associations. The imbrication of the Calzadilla ophiolite with Serie Negra took place under *P* and *T* metamorphic conditions of lower grade than in the Ribera del Fresno–Llera ophiolite, likely by means of a regional thrust structure currently concealed in a paleotectonic context neighbouring the subduction channel. There, it would have been accreted to igneous rocks from the southern magmatic arc branch reported above.

The interpretation of the Calzadilla and Ribera del Fresno–Llera ophiolites tectonic emplacement is in agreement with the currently accepted Cadomian lithosphere convergence polarity for SW Iberia. It would consist of a southern oceanic domain subducted northwards, in current coordinates (palinspastic restoration of the position of SW Iberia places it in the northern margin of Gondwana, nonetheless), with the trench located in the southern edge of the OMZ, and a back-arc basin to the other side of the northern edge (Arenas et al., 2018; Cambeses et al., 2017; Díez Fernández et al., 2019; Linnemann et al., 2014; Orejana et al., 2015). The current width and separation of the reported magmatic and metamorphic belts resulted from arc shortening and wrench displacements (related to Cadomian and Variscan orogenies) and, thus, track the original transversal dimensions of the orogenic system only to a first approximation.

8 | CONCLUSIONS

In this study, a complex polyphase history of ultramafic rock alteration, metasomatism, and tectonothermal reworking is revealed by petrochronology of chlorite-tremolite-talc rocks related to serpentinites from SW Spain. The tectonic and metasomatic processes involved include interaction with aqueous fluids in the mantle wedge (coeval with, or followed by Si and Al metasomatism), subduction channel metamorphism (postdated by early Ordovician granitoid intrusion), and intracontinental ductile shear zone reworking and isotopic resetting during the late Palaeozoic. These processes, related to a Cadomian and Variscan poly-orogenic evolution, are revealed by a so far poorly known and overlooked thrust-bounded heterogeneous ultramafic unit composed of various serpentinite types (serpentinites with antigorite overprinting lizardite mesh and ghost idiomorphic amphibole microstructures) and metasomatized rocks (chlorite-talc schists, tremolite-talc-chlorite rocks and magnesio-hornblende-chlorite ultramafic rocks).

The ultramafic rock-forming mineral phases exhibit microstructures that suggest they grew in various stages accompanied by crystal plastic deformation mechanisms under greenschist and amphibolite facies *P–T* conditions. Antigorite foliation development in the serpentinites was related to prograde reworking under HP metamorphic conditions. Mineral petrofabrics of metasomatic ultramafic rocks show significant texture intensities and reveal a close geometrical relationship with rock foliation and lineation. They are congruent among the diverse mineral phases and are associated with non-coaxial deformation components under the *P–T* conditions prevalent during their solid-state deformation. Structurally, these rocks are sandwiched between two major metamorphic thrust slices with HP Cadomian imprints.

Apatite in textural equilibrium with chlorite from ultramafic rocks provided an anchored isochron radiometric age of 342.8 ± 12.2 Ma that is consistent with syn-metamorphic reworking during the late Palaeozoic. It is disconnected from earlier serpentinization, metasomatism and HP metamorphism and highlights decoupling between isotopic systems used for radiometric dating and microstructures in metamorphic rock systems affected by distinct stages of deformation-enhanced recrystallization.

The serpentinized and metasomatized ultramafic rocks represent supra-subduction arc mantle fragments associated with metamorphic thrusts in a subduction channel, subsequently accreted to a Cadomian arc. The resultant metamorphic belt separates two parallel magmatic arc segments, a southern one with forearc affinities and a northern one with intra-arc and back-arc affinities. The associated Cadomian lithosphere convergence polarity would consist of a southern oceanic domain subducted northwards (current coordinates). Nonetheless, palinspastic restorations place SW Iberia in the northern margin of Gondwana with the oceanic domain to the north. The current width and separation of the reported magmatic and metamorphic belts resulted from arc shortening and wrench displacements during the Cadomian and Variscan orogenies. Therefore, they provide a first approximation to the original transversal dimensions of the orogenic system. In any case, its nature, geometry and dimensions can be compared to those of the southern Izu–Bonin–Mariana subduction system, which is proposed as a modern analogue of Cadomian SW Iberia.

ACKNOWLEDGEMENTS

S. García de Madinabeitia (Dep. Geology, Universidad del País Vasco-UPV/EHU, and Geochronology and Isotope Geochemistry, SGIker-UPV/EHU facility), S. Fernández-Armas (Electronic Microscopy and Material Microanalysis, SGIker-UPV/EHU facility), J. Sangüesa (Minerals and Rocks X-Ray Analysis Unit, SGIker-UPV/

EHU facility) and A. Sarmiento (Raman-LASPEA, SGIker-UPV/EHU facility) are thanked for their technical assistance with radiometric, petrofabric and mineralogical data acquisition. We gratefully thank the helpful reviews and constructive comments provided by the Journal of Metamorphic Geology anonymous reviewers, whom helped us to substantially improve this manuscript. We also thank the journal's Editor Katy Evans for her comments and editorial support. Financial support was provided by the Spanish Ministry of Economy, Industry and Competitiveness and the European Regional Development Fund (MINECO/FEDER CGL2015-63530-P), and by the UPV/EHU (GIU20/010 and GIU15/05).

ORCID

Benito Ábalos https://orcid.org/0000-0003-4690-6468
Pablo Puelles https://orcid.org/0000-0001-9687-6581
José Ignacio Gil Ibarguchi https://orcid.org/0000-0003-0279-5065

REFERENCES

Ábalos, B. (1989). Structural geology of the Ribera del Fresno window (Badajoz–Córdoba shear zone). *Revista de la Sociedad Geológica de España*, *2*, 103–112.

Ábalos, B. (1990). Cinemática y Mecanismos de la deformación en régimen de transpresión. Evolución estructural y metamórfica de la Zona de Cizalla Dúctil de Badajoz–Córdoba. Ph. D Thesis. Universidad del País Vasco.

Ábalos, B. (1992). Variscan shear-zone deformation of late Precambrian basement in SW Iberia: Implications for circum-Atlantic pre-Mesozoic tectonics. *Journal of Structural Geology*, *14*, 807–823. https://doi.org/10.1016/0191-8141(92)90042-U

Ábalos, B., & Cusí, J. D. (1995). Correlation between seismic anisotropy and major geological structures in SW Iberia: A case study on continental lithosphere deformation. *Tectonics*, *14*, 1021–1040. https://doi.org/10.1029/95TC01204

Ábalos, B., Gil Ibarguchi, J. I., & Eguiluz, L. (1991). Cadomian subduction/collision and Variscan transpression in the Badajoz–Córdoba shear belt, Southwest Spain. *Tectonophysics*, *199*, 51–72. https://doi.org/10.1016/0040-1951(91)90118-C

Abati, J., Arenas, R., Díez Fernández, R., Albert, R., & Gerdes, A. (2018). Combined zircon U–Pb and Lu–Hf isotopes study of magmatism and high-P metamorphism of the basal allochthonous units in the SW Iberian massif (Ossa-Morena complex). *Lithos*, *322*, 20–37. https://doi.org/10.1016/j.lithos.2018.07.032

Abranches, M. C. B., Canilho, M. H., & Canelhas, M. G. S. (1979). Nota preliminar sobre a idade absoluta pelo método do Rb/Sr dos granitos do Porto e de Portalegre. *Boletim Da Sociedade Geológica de Portugal*, *XXI*, 2–3.

Aertgeerts, G., Lorand, J. P., Monnier, C., & La, C. (2018). Petrogenesis of south Armorican serpentinized peridotites. *Lithos*, *314–315*, 100–118. https://doi.org/10.1016/j.lithos.2018.05.013

Agard, P., Yamato, P., Jolivet, L., & Burov, E. (2009). Exhumation of oceanic blueschists and eclogites in subduction zones: Timing and mechanisms. *Earth-Science Reviews*, *92*, 53–79. https://doi.org/10.1016/j.earscirev.2008.11.002

Aguayo, J. (1985). *Rocas ultramáficas en el sector de Calzadilla de los Barros (Badajoz)*. Universidad del País Vasco.

Akker, I. V., Tajčmanová, L., Marques, F. O., & Burg, J. P. (2020). U–Pb zircon geochronology and phase equilibria modelling of HP-LT rocks in the Ossa-Morena zone, Portugal. *International Journal of Earth Sciences*, *109*, 2719–2738. https://doi.org/10.1007/s00531-020-01921-w

Amiguet, E., Van De Moortèle, B., Cordier, P., Hilairet, N., & Reynard, B. (2014). Deformation mechanisms and rheology of serpentines in experiments and in nature. *Journal of Geophysical Research*, *119*, 4640–4655. https://doi.org/10.1002/2013JB010791

Angiboust, S., Agard, P., Raimbourg, H., Yamato, P., & Huet, B. (2011). Subduction interface processes recorded by eclogite-facies shear zones (Monviso, W. Alps). *Lithos*, *127*, 222–238. https://doi.org/10.1016/j.lithos.2011.09.004

Apalategui, O., Eguíluz, L., & Quesada, C. (1990). Ossa-Morena zone: 3. Structure. In R. D. Dallmeyer & E. Martínez-García (Eds.), *Pre-Mesozoic geology of Iberia* (pp. 280–292). Springer-Verlag. https://doi.org/10.1007/978-3-642-83980-1_18

Apalategui, O., & Higueras, P. (1983). Mapa y memoria explicativa de la Hoja 1:50.000, N° 855 (Usagre) del Mapa Geológico Nacional (MAGNA). Madrid.

Apalategui, O., Higueras, P., Contreras, F., Arriola, A., Garrote, A., Eguíluz, L., & Sánchez-Carretero, R. (1988). Mapa y memoria explicativa de la Hoja 1:50.000, N° 830 (Hornachos) del Mapa Geológico Nacional (MAGNA). Madrid.

Apalategui, O., & Quesada, C. (1987). Transversal Geológica Zona de Ossa-Morena. Libro-Guía Excursión IGME-Ossa-Morena (Aracena-Zafra). *Publications of the Instituto Geológico y Minero de España*. Madrid.

Arenas, R., Fernández-Suárez, J., Montero, P., Díez Fernández, R., Andonaegui, P., Sánchez Martínez, S., Albert, R., Fuenlabrada, J. M., Matas, J., Martín Parra, L. M., Rubio Pascual, F. J., Jiménez-Díaz, A., & Pereira, M. F. (2018). The Calzadilla ophiolite (SW Iberia) and the Ediacaran fore-arc evolution of the African margin of Gondwana. *Gondwana Research*, *58*, 71–86. https://doi.org/10.1016/j.gr.2018.01.015

Arenas, R., Novo-Fernández, I., Garcia-Casco, A., Díez Fernández, R., Fuenlabrada, J. M., Pereira, M. F., Abati, J., Sánchez Martínez, S., & Rubio Pascual, F. J. (2020). A unique blueschist facies metapelite with Mg-rich chloritoid from the Badajoz–Córdoba unit (SW Iberian massif): Correlation of Late Devonian high-pressure belts along the Variscan Orogen. *International Geology Review*, *63*, 1634–1657. https://doi.org/10.1080/00206814.2020.1789509

Arriola, A., Chacón, J., Eraso, A., Eguíluz, L., Garrote, A., Soubrier, R., & Vargas, I. (1983). Mapa y memoria explicativa de la Hoja 1:50.000, N° 829 (Villafranca de los Barros) del Mapa Geológico Nacional (MAGNA). Madrid.

Arriola, A., Cueto, L. A., Fernández Carrasco, J., & Garrote, A. (1983). Serpentinitas y mineralizaciones de cromo asociadas, en el Proterozoico Superior de Ossa-Morena. *Cuadernos Del Laboratorio Geológico de Laxe*, *8*, 137–146.

Arriola, A., Garrote, A., Eguíluz, L., Sánchez-Carretero, R., & Fernández Carrasco, J. (1983). Mapa y memoria explicativa de

la Hoja 1:50.000, N° 876 (Fuente de Cantos) del Mapa Geológico Nacional (MAGNA). Madrid.

Aupart, C., Morales, L., Godard, M., Jamtveit, B., & the Oman DP Science Team. (2021). Seismic faults triggered early stage serpentinization of peridotites from the Samail ophiolite, Oman. *Earth and Planetary Science Letters*, *574*, 117–137. https://doi.org/10.1016/j.epsl.2021.117137

Auzende, A.-L., Guillot, S., Devouard, B., & Baronnet, A. (2006). Serpentinites in an Alpine convergent setting: Effects of metamorphic grade and deformation on microstructures. *European Journal of Mineralogy*, *18*, 21–33. https://doi.org/10.1127/0935-1221/2006/0018-0021

Azor, A. (1994). *Evolución Tectonometamórfica del limite ente las zonas Centroibérica y de Ossa-Morena (Cordillera Varisca, SO de España)*. Universidad de Granada.

Azor, A., González Lodeiro, F., & Simancas, J. F. (1994). Tectonic evolution of the boundary between the central Iberian and Ossa-Morena zones (Variscan belt, Southwest Spain). *Tectonics*, *13*, 45–61. https://doi.org/10.1029/93TC02724

Azor, A., Martínez-Poyatos, D., Montero, P., González-Lodeiro, J. F., & Pérez-Cáceres, I. (2016). U-Pb zircon age and tectonic meaning of the Cardenchosa pluton (Ossa-Morena zone). *IX Congreso Geológico de España. Geotemas*, *16*(2), 23–26.

Azor, A., Simancas, F., Martínez Poyatos, D., & González Lodeiro, F. (2022). Comment on "on the rootless nature of a Devonian suture in SW Iberia (Ossa-Morena complex, Variscan Orogen): Geometry and kinematics of the Azuaga fault" by Díez Fernández et al. (2021). *Tectonics*, *41*, e2021TC006982. https://doi.org/10.1029/2021TC006982

Bandrés, A., Eguíluz, L., Gil Ibarguchi, J. I., & Palacios, T. (2002). Geodynamic evolution of a Cadomian arc region: The northern Ossa-Morena zone, Iberian massif. *Tectonophysics*, *352*, 105–120. https://doi.org/10.1016/S0040-1951(02)00191-9

Bandrés, A., Eguíluz, L., Pin, C., Paquette, J. L., Ordóñez, B., Le Fèvre, B., Ortega, L. A., & Gil Ibarguchi, J. I. (2004). The northern Ossa-Morena Cadomian batholith (Iberian massif): Magmatic arc origin and early evolution. *International Journal of Earth Sciences*, *93*(5), 860–885. https://doi.org/10.1007/s00531-004-0423-6

Baratoux, L., Schulmann, K., Ulrich, S., & Lexa, O. (2005). Contrasting microstructures and deformation mechanisms in metagabbro mylonites contemporaneously deformed under different temperatures (c. 650°C and c. 750°C). *Geological Society Special Publication*, *243*, 97–125. https://doi.org/10.1144/GSL.SP.2005.243.01.09

Barber, D. J., Wenk, H. R., Hirth, G., & Kohlstedt, D. L. (2010). Dislocations in Minerals. In L. Hirth & J. P. Kubin (Eds.), *Dislocations in solids* (Vol. 19) (pp. 171–232). Elsevier. https://doi.org/10.1016/S1572-4859(09)01604-0

Bellon, H., Blanchére, H., Crousilles, M., Deloche, C., Dixsaut, C., Hertritch, B., Prost-Dame, V., Rossi, P., Simon, D., & Tamain, G. (1979). Radiochronologie, évolution téctono-magmatique et implications métallogéniques dans les cadomo-variscides du Sud-Est Hespérique. *Bulletin de La Societé Géologique de France*, *21*, 113–120. https://doi.org/10.2113/gssgfbull.S7-XXI.2.113

Beranoaguirre, A., Puelles, P., Ábalos, B., Gil Ibarguchi, J. I., & García de Madinabeitia, S. (2019). Short-duration regional metamorphic event recorded in a Variscan subduction channel (Malpica–Tui eclogites, NW Iberia). *International Journal of Earth Sciences*, *108*, 2037–2046. https://doi.org/10.1007/s00531-019-01747-1

Bezacier, L., Reynard, B., Bass, J. D., Sánchez Valle, C., & Van de Moortèle, B. (2010). Elasticity of antigorite, seismic detection of serpentinites, and anisotropy in subduction zones. *Earth and Planetary Science Letters*, *289*, 198–208. https://doi.org/10.1016/j.epsl.2009.11.009

Biermann, C., & Van Roermund, H. L. M. (1983). Defect structures in naturally deformed clinoamphiboles-a TEM study. *Tectonophysics*, *95*, 267–278. https://doi.org/10.1016/0040-1951(83)90072-0

Blatrix, P., & Burg, J. P. (1981). 40Ar-40Ar dates from Sierra Morena (southern Spain). Variscan metamorphism and Cadomian orogeny. *Neues Jahrbuch für Mineralogie Monatshefte*, *10*, 470–478.

Bons, A. J. (1988). Deformation of chlorite in naturally deformed low-grade rocks. *Tectonophysics*, *154*, 149–165. https://doi.org/10.1016/0040-1951(88)90232-6

Boschi, C., Früh-Green, G. L., & Escartín, J. (2006). Occurrence and significance of serpentinite-hosted, talc- and amphibole-rich fault rocks in modern oceanic settings and ophiolite complexes: An overview. *Ofioliti*, *31*, 129–140. https://doi.org/10.4454/ofioliti.v31i2.335

Boudier, F., Baronnet, A., & Mainprice, D. (2010). Serpentine mineral replacements of natural olivine and their seismic implications: Oceanic Lizardite versus subduction-related antigorite. *Journal of Petrology*, *51*, 495–512. https://doi.org/10.1093/petrology/egp049

Bouzari, F., Hart, C. J. R., Bissig, T., & Barker, S. (2016). Hydrothermal alteration revealed by apatite luminescence and chemistry: A potential indicator mineral for exploring covered porphyry copper deposits. *Economic Geology*, *111*, 1397–1410. https://doi.org/10.2113/econgeo.111.6.1397

Bunge, H. J. (1982). *Texture Analysis in Materials Science: Mathematical methods* (p. 593). Butterworths. https://doi.org/10.1016/B978-0-408-10642-9.50019-2

Burg, J. P., Iglesias, M., Laurent, P., Matte, P., & Ribeiro, A. (1981). Variscan intracontinental deformation: The Coimbra-Córdoba shear zone (SW Iberian Peninsula). *Tectonophysics*, *78*, 161–177. https://doi.org/10.1016/0040-1951(81)90012-3

Cambeses, A., Scarrow, J. H., Montero, P., Lázaro, C., & Bea, F. (2017). Palaeogeography and crustal evolution of the Ossa–Morena zone, Southwest Iberia, and the North Gondwana margin during the Cambro-Ordovician: A review of isotopic evidence. *International Geology Review*, *59*, 94–130. https://doi.org/10.1080/00206814.2016.1219279

Chacón, J. (1979). *Estudio geológico del sector central del anticlinorio Portalegre-Badaloz-Córdoba (Macizo Ibérico Meridional)*. Universidad de Granada.

Chacón, J., & Velasco, F. (1981). Rocas ultrabásicas metamorfizadas en el Grupo de Azuaga (Anticlinorio Badajoz–Córdoba). *Cuadernos de Geología Ibérica*, *7*, 151–159.

Cochrane, R., Spikings, R. A., Chew, D., Wotzlaw, J. F., Chiaradia, M., Tyrrell, S., Schaltegger, U., & Van der Lelij, R. (2014). High temperature (>350°C) thermochronology and mechanisms of Pb loss in apatite. *Geochimica et Cosmochimica Acta*, *127*, 39–56. https://doi.org/10.1016/j.gca.2013.11.028

Corfu, F., & Stone, D. (1998). The significance of titanite and apatite U-Pb ages: Constraints for the post-magmatic thermal-hydrothermal evolution of a batholithic complex, Berens River area, northwestern Superior Province, Canada. *Geochimica et Cosmochimica Acta*, *62*, 2979–2995. https://doi.org/10.1016/S0016-7037(98)00225-7

Cumbest, R. J., Drury, M. R., van Roermund, H. L. M., & Simpson, C. (1989). Dynamic recrystallization and chemical evolution of clinoamphibole from Senja, Norway. *Contributions to Mineralogy and Petrology*, *101*, 339–349. https://doi.org/10.1007/BF00375318

Dale, J., Holland, T., & Powell, R. (2000). Hornblende-garnet-plagioclase thermobarometry: A natural assemblage calibration of the thermodynamics of hornblende. *Contributions to Mineralogy and Petrology*, *140*, 353–362. https://doi.org/10.1007/s004100000187

Dallmeyer, R. D., & Martínez-García, E. (1990). *Pre-Mesozoic geology of Iberia*. Springer-Verlag. https://doi.org/10.1007/978-3-642-83980-1

Díez Fernández, R., & Arenas, R. (2015). The late Devonian Variscan suture of the Iberian massif: A correlation of high-pressure belts in NW and SW Iberia. *Tectonophysics*, *654*, 96–100. https://doi.org/10.1016/j.tecto.2015.05.001

Díez Fernández, R., Arenas, R., Pereira, M. F., Sánchez-Martínez, S., Albert, R., Martín Parra, L. M., Rubio-Pascual, F. J., & Matas, J. (2016). Tectonic evolution of Variscan Iberia: Gondwana–Laurussia collision revisited. *Earth-Science Reviews*, *162*, 269–292. https://doi.org/10.1016/j.earscirev.2016.08.002

Díez Fernández, R., Fernández, C., Arenas, R., & Novo-Fernández, I. (2021). On the rootless nature of a Devonian suture in SW Iberia (Ossa-Morena complex, Variscan orogen): Geometry and kinematics of the Azuaga fault. *Tectonics*, *40*, e2021TC006791. https://doi.org/10.1129/2021TC006791

Díez Fernández, R., Fernández, C., Arenas, R., & Novo-Fernández, I. (2022). Reply to comment by Azor et al. on "On the rootless nature of a Devonian suture in SW Iberia (Ossa-Morena complex, Variscan orogen): Geometry and kinematics of the Azuaga fault". *Tectonics*, *41*, e2021TC007154. https://doi.org/10.1029/2021TC007154

Díez Fernández, R., Jiménez-Díaz, A., Arenas, R., Pereira, M. F., & Fernández-Suárez, J. (2019). Ediacaran Obduction of a fore-arc ophiolite in SW Iberia: A turning point in the evolving geodynamic setting of Peri-Gondwana. *Tectonics*, *38*, 95–119. https://doi.org/10.1029/2018TC005224

Dollinger, G., & Blacic, J. D. (1975). Deformation mechanisms in experimentally and naturally deformed amphiboles. *Earth and Planetary Science Letters*, *26*, 409–416. https://doi.org/10.1016/0012-821X(75)90016-3

Droop, G. (1987). A general equation for estimating Fe3+ concentrations in ferromagnesian silicates and oxides from microprobe analyses, using stoichiometric criteria. *Mineralogical Magazine*, *51*, 431–435. https://doi.org/10.1180/minmag.1987.051.361.10

Dymek, R. F., Brothers, S. C., & Schiffries, C. M. (1988). Petrogenesis of ultramafic metamorphic rocks from the 3800 Ma Isua Supracrustal Belt, West Greenland. *Journal of Petrology*, *29*, 1353–1397. https://doi.org/10.1093/petrology/29.6.1353

Eguíluz, L., Gil Ibarguchi, J. I., Ábalos, B., & Apraiz, A. (2000). Superposed Hercynian and Cadomian orogenic cycles in the Ossa-Morena zone and related areas of the Iberian massif. *Bulletin of the Geological Society of America*, *112*, 1398–1413. https://doi.org/10.1130/0016-7606(2000)112<1398:SHACOC>2.0.CO;2

Epstein, G. S., Bebout, G. E., & Angiboust, S. (2021). Fluid and mass transfer along transient subduction interfaces in a deep paleo-accretionary wedge (Western Alps). *Chemical Geology*, *559*, 119920. https://doi.org/10.1016/j.chemgeo.2020.119920

Escartín, J., Andreani, M., Hirth, G., & Evans, B. (2008). Relationships between the microstructural evolution and the rheology of talc at elevated pressures and temperatures. *Earth and Planetary Science Letters*, *268*, 463–475. https://doi.org/10.1016/j.epsl.2008.02.004

Escartín, J., Mével, C., MacLeod, C. J., & McCaig, A. M. (2003). Constraints on deformation conditions and the origin of oceanic detachments: The mid-Atlantic ridge core complex at 15°45′N. *Geochemistry, Geophysics, Geosystems*, *4*, 1067. https://doi.org/10.1029/2002GC000472

Evans, B. W. (1977). Metamorphism of alpine peridotite and serpentinite. *Annual Review of Earth and Planetary Sciences*, *5*, 397–447. https://doi.org/10.1146/annurev.ea.05.050177.002145

Evans, B. W. (2004). The serpentinite multisystem revisited: Chrysotile is metastable. *International Geology Review*, *46*, 479–506. https://doi.org/10.2747/0020-6814.46.6.479

Evans, B. W., Hattori, K., & Baronnet, A. (2013). Serpentinite: What, why, where? *Elements*, *9*, 99–106. https://doi.org/10.2113/gselements.9.2.99

Frost, B. R., & Beard, J. S. (2007). On silica activity and serpentinization. *Journal of Petrology*, *48*, 1351–1368. https://doi.org/10.1093/petrology/egm021

García-Casquero, J. L., Priem, H. N. A., Boelrijk, N. A. I. M., & Chacon, J. (1988). Isotopic dating of the mylonitization of the Azuaga Group in the Badajóz-Córdoba belt, SW Spain. *Geologische Rundschau*, *77*, 483–489. https://doi.org/10.1007/BF01832393

Gordon, S. M., Kirkland, C. L., Reddy, S. M., Blatchford, H. J., Whitney, D. L., Teyssier, C., Evans, N. J., & McDonald, B. J. (2021). Deformation-enhanced recrystallization of titanite drives decoupling between U-Pb and trace elements. *Earth and Planetary Science Letters*, *560*, 116810. https://doi.org/10.1016/j.epsl.2021.116810

Guillot, S., Hattori, K., Agard, P., Schwartz, S., & Vidal, O. (2009). Exhumation processes in oceanic and continental subduction contexts: A review. *In S. Lallemand and F. Funiciello (eds.), Subduction Zone Geodynamics*, 175–205. https://doi.org/10.1007/978-3-540-87974-9_10

Guillot, S., Schwartz, S., Reynard, B., Agard, P., & Prigent, C. (2015). Tectonic significance of serpentinites. *Tectonophysics*, *646*, 1–19. https://doi.org/10.1016/j.tecto.2015.01.020

Hall, J. W., Glorie, S., Reid, A. J., Boone, S. C., Collins, A. S., & Gleadow, A. (2018). An apatite U–Pb thermal history map for the northern Gawler craton, South Australia. *Geoscience Frontiers*, *9*, 1293–1308. https://doi.org/10.1016/j.gsf.2017.12.010

Harlov, D. E., Wirth, R., & Förster, H. J. (2005). An experimental study of dissolution-reprecipitation in fluorapatite: Fluid infiltration and the formation of monazite. *Contributions to*

Mineralogy and Petrology, *150*, 268–286. https://doi.org/10.1007/s00410-005-0017-8

Hawthorne, F. C., Oberti, R., Harlow, G. E., Maresch, W. V., Martin, R. F., Schumacher, J. V., & Welch, M. D. (2012). Nomenclature of the amphibole supergroup. *American Mineralogist*, *97*, 2031–2048. https://doi.org/10.2138/am.2012.4276

Herranz, P. (1984). El Precámbrico y su cobertera paleozoica en la región centro-oriental de la Provincia de Badajoz. Ph. D Thesis. Universidad Complutense de Madrid.

Herranz, P. (1985). *El Precámbrico y su cobertera paleozoica en la región centro-oriental de la Provincia de Badajoz*. Seminarios de Estratigrafía, Serie Monografías, 10, vols. 1 (p. 1–341), 2 (p. 342–833), 3 (p. 834–1220) and 4 (p. 1221–1342). Universidad Computense.

Hess, H. H. (1933). The problem of serpentinization and the origin of certain chrysotile asbestos, talc and soapstone deposits. *Economic Geology*, *28*, 634–657. https://doi.org/10.2113/gsecongeo.28.7.634

Hey, M. H. (1954). A new review of the chlorites. *Mineralogical Magazine and Journal of the Mineralogical Society*, *30*, 277–292. https://doi.org/10.1180/minmag.1954.030.224.01

Hirauchi, K., Michibayashi, K., Ueda, H., & Katayama, I. (2010). Spatial variations in antigorite fabric across a serpentinite subduction channel: Insights from the Ohmachi seamount, Izu-Bonin frontal arc. *Earth and Planetary Science Letters*, *299*, 196–206. https://doi.org/10.1016/j.epsl.2010.08.035

Holland, T., & Blundy, J. (1994). Non-ideal interactions in calcic amphiboles and their bearing on amphibole-plagioclase thermometry. *Contributions to Mineralogy and Petrology*, *116*, 433–447. https://doi.org/10.1007/BF00310910

Hyndman, R. D., & Peacock, S. M. (2003). Serpentinization of the forearc mantle. *Earth and Planetary Science Letters*, *212*, 417–432. https://doi.org/10.1016/S0012-821X(03)00263-2

Ichiyama, Y., Tsujimori, T., Fryer, P., Michibayashi, K., Tamura, A., & Morishita, T. (2021). Temporal and spatial mineralogical changes in clasts from the Mariana serpentinite mud volcanoes: Cooling of the hot forearc-mantle at subduction initiation. *Lithos*, *384-385*, 105941. https://doi.org/10.1016/j.lithos.2020.105941

Iyer, K. (2007). Mechanics of serpentinization and some geochemical effects. Ph. D Thesis. University of Oslo.

Jacobson, C. E. (1989). Estimation of Fe 3+ from electron microprobe analyses: Observations on calcic amphibole and chlorite. *Journal of Metamorphic Geology*, *7*, 507–513. https://doi.org/10.1111/j.1525-1314.1989.tb00613.x

Ji, S., Li, A., Wang, Q., Long, C., Wang, H., Marcotte, D., & Salisbury, M. (2013). Seismic velocities, anisotropy, and shear-wave splitting of antigorite serpentinites and tectonic implications for subduction zones. *Journal of Geophysical Research: Solid Earth*, *118*, 1015–1037. https://doi.org/10.1002/jgrb.50110

Jiménez-Díaz, A. (2008). Análisis de los procesos de cizalla dúctil en el macizo peridotítico de Calzadilla de los Barros (Extremadura). Ms.Sc. Thesis. Universidad Complutense de Madrid Madrid.

Jiménez-Díaz, A., Capote, R., Tejero, R., Lunar, R., Ortega, L., Monterrubio, S., Maldinaco, C., & Rodríguez, D. (2009). La fábrica de las rocas miloníticas de la Zona de Cizalla de Los Llanos (Calzadilla de los Barros, Badajoz) - E-Prints Complutense. *Geogaceta*, *46*, 27–30. https://eprints.ucm.es/id/eprint/10958/

Jung, H. (2011). Seismic anisotropy produced by serpentine in mantle wedge. *Earth and Planetary Science Letters*, *307*, 535–543. https://doi.org/10.1016/j.epsl.2011.05.041

Kang, H., & Jung, H. (2019). Lattice-preferred orientation of amphibole, chlorite, and olivine found in hydrated mantle peridotites from Bjørkedalen, southwestern Norway, and implications for seismic anisotropy. *Tectonophysics*, *750*, 137–152. https://doi.org/10.1016/j.tecto.2018.11.011

Katayama, I., Hirauchi, K. I., Michibayashi, K., & Ando, J. I. (2009). Trench-parallel anisotropy produced by serpentine deformation in the hydrated mantle wedge. *Nature*, *461*, 1114–1117. https://doi.org/10.1038/nature08513

Kim, D., & Jung, H. (2015). Deformation microstructures of olivine and chlorite in chlorite peridotites from Almklovdalen in the Western Gneiss Region, Southwest Norway, and implications for seismic anisotropy. *International Geology Review*, *57*, 650–668. https://doi.org/10.1080/00206814.2014.936054

Kim, D., Jung, H., & Lee, J. (2020). Strain-induced fabric transition of chlorite and implications for seismic anisotropy in subduction zones. *Minerals*, *10*, 503. https://doi.org/10.3390/min10060503

Kirkland, C. L., Yakymchuk, C., Szilas, K., Evans, N., Hollis, J., McDonald, B., & Gardiner, N. J. (2018). Apatite: A U-Pb thermochronometer or geochronometer? *Lithos*, *318–319*, 143–157. https://doi.org/10.1016/j.lithos.2018.08.007

Ko, B., & Jung, H. (2015). Crystal preferred orientation of an amphibole experimentally deformed by simple shear. *Nature Communications*, *6*, 1–10. https://doi.org/10.1038/ncomms7586

Kohli, A. H., Goldsby, D. L., Hirth, G., & Tullis, T. (2011). Flash weakening of serpentinite at near-seismic slip rates. *Journal of Geophysical Research: Solid Earth*, *116*, B03202. https://doi.org/10.1029/2010JB007833

Krestianinov, E., Amelin, Y., Neymark, L. A., & Aleinikoff, J. N. (2021). U-Pb systematics of uranium-rich apatite from Adirondacks: Inferences about regional geological and geochemical evolution, and evaluation of apatite reference materials for in situ dating. *Chemical Geology*, *581*, 120417. https://doi.org/10.1016/j.chemgeo.2021.120417

Laird, J., & Albee, A. L. (1981). Pressure, temperature, and time indicators in mafic schist; their application to reconstructing the polymetamorphic history of Vermont. *American Journal of Science*, *281*, 127–175. https://doi.org/10.2475/ajs.281.2.127

Leake, B. E., Woolley, A. R., Arps, C. E. S., Birch, W. D., Gilbert, M. C., Grice, J. D., Hawthorne, F. C., Kato, A., Kisch, H. J., Krivovichev, V. G., Linthout, K., Laird, J., Mandarino, J. A., Maresch, W. V., Nickel, E. H., Rock, N. M. S., Schumacher, J. C., Smith, D. C., Stephenson, N. C. N., ... Youzhi, G. (1997). Nomenclature of amphiboles: Report of the subcommittee on amphiboles of the international mineralogical association, commission on new minerals and mineral names. *American Mineralogist*, *61*, 295–310. https://doi.org/10.1180/minmag.1997.061.405.13

Linnemann, U., Gerdes, A., Hofmann, M., & Marko, L. (2014). The Cadomian Orogen: Neoproterozoic to Early Cambrian crustal growth and orogenic zoning along the periphery of the West African craton-constraints from U-Pb zircon ages and Hf

isotopes (Schwarzburg Antiform, Germany). *Precambrian Research*, *244*, 236–278. https://doi.org/10.1016/j.precamres.2013.08.007

López Sánchez-Vizcaíno, V., Gómez-Pugnaire, M. T., Azor, A., & Fernández-Soler, J. M. (2003). Phase diagram sections applied to amphibolites: A case study from the Ossa-Morena/Central Iberian Variscan suture (southwestern Iberian massif). *Lithos*, *68*, 1–21. https://doi.org/10.1016/S0024-4937(03)00017-3

López-Guijarro, R., Armendáriz, M., Quesada, C., Fernández-Suárez, J., Murphy, J. B., Pin, C., & Bellido, F. (2008). Ediacaran-Palaeozoic tectonic evolution of the Ossa Morena and Central Iberian zones (SW Iberia) as revealed by Sm-Nd isotope systematics. *Tectonophysics*, *461*, 202–214. https://doi.org/10.1016/j.tecto.2008.06.006

Martínez-Catalán, J. R., Schulmann, K., & Ghienne, J.-F. (2021). The mid-Variscan allochthon: Keys from correlation, partial retrodeformation and plate-tectonic reconstruction to unlock the geometry of a non-cylindrical belt. *Earth-Science Reviews*, *220*, 103700. https://doi.org/10.1016/j.earscirev.2021.103700

Martínez-García, E., Herranz, P., de San José, M. A., Perejón, A., González-Casado, J. M., Pieren, A., Apalategui, O., Eguíluz, L., & Hernández-Enrile, J. L. (1986). Geotraverse south (B-1) Excursión guidebook (7–13 September, 1986).

Martos, R., Ortega, L., Gervilla, F., Piña, R., Monterrubio, S., Lunar, R., & Albert, H. (2010). Caracterización químico-mineralógica de las cromititas ofiolíticas de Calzadilla de los Barros (Badajoz). *Geogaceta*, *48*, 175–175.

Moore, D. E., & Rymer, M. J. (2007). Talc-bearing serpentinite and the creeping section of the San Andreas fault. *Nature*, *448*, 795–797. https://doi.org/10.1038/nature06064

Morrow, C. A., Moore, D. E., & Lockner, D. A. (2000). The effect of mineral bond strength and adsorbed water on fault gouge frictional strength. *Geophysical Research Letters*, *27*, 815–818. https://doi.org/10.1029/1999GL008401

Nagaya, T., Okamoto, A., Oyanagi, R., Seto, Y., Miyake, A., Uno, M., Muto, J., & Wallis, S. R. (2020). Crystallographic preferred orientation of talc determined by an improved EBSD procedure for sheet silicates: Implications for anisotropy at the slab-mantle interface due to Si-metasomatism. *American Mineralogist*, *105*, 873–893. https://doi.org/10.2138/am-2020-7006

Nakano, T., Awazu, T., & Umakoshi, Y. (2001). Plastic deformation and operative slip system in mineral fluorapatite single crystal. *Scripta Materialia*, *44*, 811–815. https://doi.org/10.1016/S1359-6462(00)00656-4

Nishii, A., Wallis, S. R., Mizukami, T., & Michibayashi, K. (2011). Subduction related antigorite CPO patterns from forearc mantle in the Sanbagawa belt, Southwest Japan. *Journal of Structural Geology*, *33*, 1436–1445. https://doi.org/10.1016/j.jsg.2011.08.006

Ochsner, A. (1993). U-Pb geochronology of the Upper Proterozoic - Lower Paleozoic geodynamic evolution in the Ossa-Morena zone (SW Iberia): Constraints on the timing of the Cadomian orogeny. PhD. Dissertation. Eidgenössische Technische Hoschschule, Zürich, Switzerland.

Ochsner, A., Schäffer, H.-J., & Gebauer, D. (1992). The geochemistry and age of granitoids of the Ossa-Morena zone (SW Spain): Implications for the Late Precambrian and Early Paleozoic geodynamic evolution. *Publicaciones Del Museo de Geología de Extremadura*, *1*, 113.

Ordóñez-Casado, B. (1998). Geochronological studies of the pre-Mesozoic basement of the Iberian massif: The Ossa Morena zone and the allochthonous complexes within the central Iberian zone. PhD. Dissertation. Eidgenössische Technische Hoschschule, Zürich, Switzerland.

Orejana, D., Merino Martínez, E., Villaseca, C., & Andersen, T. (2015). Ediacaran-Cambrian paleogeography and geodynamic setting of the central Iberian zone: Constraints from coupled U-Pb-Hf isotopes of detrital zircons. *Precambrian Research*, *261*, 234–251. https://doi.org/10.1016/j.precamres.2015.02.009

Ouadahi, S., Bendaoud, A., Bodinier, J.-L., Dautria, J. M., Vauchez, A., Fettous, E.-H., & Alard, O. (2022). A suture related accretionary wedge in the Gondwana assembly: Insights from serpentinites in the Hoggar shield, Algeria. *Precambrian Research*, *369*, 106505. https://doi.org/10.1016/j.precamres.2021.106505

Padrón-Navarta, J. A., López Sánchez-Vizcaino, V., Hermann, J., Connolly, J. A. D., Garrido, C. J., Gomez-Pugnaire, M. T., & Marchesi, C. (2013). Tschermak's substitution in antigorite and consequences for phase relations and water liberation in high-grade serpentinites. *Lithos*, *178*, 186–196. https://doi.org/10.1016/j.lithos.2013.02.001

Pereira, M. F., Chichorro, M., Solá, A. R., Silva, J. B., Sánchez-García, T., & Bellido, F. (2011). Tracing the Cadomian magmatism with detrital/inherited zircon ages by in-situ U-Pb SHRIMP geochronology (Ossa-Morena zone, SW Iberian massif). *Lithos*, *123*, 204–217. https://doi.org/10.1016/j.lithos.2010.11.008

Picazo, S., Manatschal, G., Cannat, M., & Andréani, M. (2013). Deformation associated to exhumation of serpentinized mantle rocks in a fossil ocean continent transition: The Totalp unit in SE Switzerland. *Lithos*, *175–176*, 255–271. https://doi.org/10.1016/j.lithos.2013.05.010

Pin, C., Liñán, E., Pascual, E., Donaire, T., & Valenzuela, A. (2002). Late Neoproterozoic crustal growth in the European Variscides: Nd isotope and geochemical evidence from the Sierra de Córdoba andesites (Ossa-Morena zone, southern Spain). *Tectonophysics*, *352*, 133–151. https://doi.org/10.1016/S0040-1951(02)00193-2

Pognante, U. (1989). Early Alpine eclogitisation in talc/chloritoid-bearing Mg-metagabbros and in jadeite-Fe-omphacite-bearing metatrondhjemites from the ophiolites of the Western Alps. *Rendiconti Della Società Italiana Di Mineralogia e Petrologia*, *43*, 687–704.

Puelles, P., Ábalos, B., Gil Ibarguchi, J. I., Sarrionandia, F., Carracedo, M., & Fernández-Armas, S. (2016). Petrofabric and seismic properties of lithospheric mantle xenoliths from the Calatrava volcanic field (Central Spain). *Tectonophysics*, *683*, 200–215. https://doi.org/10.1016/j.tecto.2016.06.032

Puelles, P., Gil Ibarguchi, J. I., Beranoaguirre, A., & Ábalos, B. (2012). Mantle wedge deformation recorded by high-temperature peridotite fabric superposition and hydrous retrogression (Limo massif, Cabo Ortegal, NW Spain). *International Journal of Earth Sciences*, *101*, 1835–1853. https://doi.org/10.1007/s00531-012-0761-8

Quesada, C. (1990). Precrambrian terranes in the Iberian Variscan foldbelt. In *Avalonian and Cadomian geology of the North*

Atlantic (pp. 109–133). Springer Netherlands. https://doi.org/10.1007/978-94-009-0401-9_7

Quesada, C., & Dallmeyer, R. D. (1994). Tectonothermal evolution of the Badajoz–Cordóba shear zone (SW Iberia): Characteristics and 40Ar/39Ar mineral age constraints. *Tectonophysics*, *231*, 195–213. https://doi.org/10.1016/0040-1951(94)90130-9

Rampone, E., Piccardo, G. B., Vannucci, R., Bottazzi, P., & Ottolini, L. (1993). Subsolidus reactions monitored by trace element partitioning: The spinel- to plagioclase-facies transition in mantle peridotites. *Contributions to Mineralogy and Petrology*, *115*, 1–17. https://doi.org/10.1007/BF00712974

Reynard, B. (2013). Serpentine in active subduction zones. *Lithos*, *178*, 171–185. https://doi.org/10.1016/j.lithos.2012.10.012

Reynard, B., Gillet, P., & Willaime, C. (1989). Deformation mechanisms in naturally deformed glaucophanes: A TEM and HREM study. *European Journal of Mineralogy*, *1*(5), 611–624. https://doi.org/10.1127/ejm/1/5/0611

Ribeiro, A., Quesada, C., & Dallmeyer, R. D. (1990). Geodynamic evolution of the Iberian massif. In *Pre-Mesozoic geology of Iberia* (pp. 399–409). Springer Berlin Heidelberg. https://doi.org/10.1007/978-3-642-83980-1_28

Ribeiro, B. V., Lagoeiro, L., Faleiros, F. M., Hunter, N. J. R., Queiroga, G., Raveggi, M., Cawood, P. A., Finch, M., & Campanha, G. A. C. (2020). Strain localization and fluid-assisted deformation in apatite and its influence on trace elements and U–Pb systematics. *Earth and Planetary Science Letters*, *545*, 116421. https://doi.org/10.1016/j.epsl.2020.116421

Rojo-Pérez, E., Arenas, R., Fuenlabrada, J. M., Sánchez Martínez, S., Martín Parra, L. M., Matas, J., Pieren, A. P., & Díez Fernández, R. (2019). Contrasting isotopic sources (Sm-Nd) of Late Ediacaran series in the Iberian massif: Implications for the central Iberian-Ossa Morena boundary. *Precambrian Research*, *324*, 194–207. https://doi.org/10.1016/j.precamres.2019.01.021

Rojo-Pérez, E., Fuenlabrada, J. M., Linnemann, U., Arenas, R., Sánchez Martínez, S., Díez Fernández, R., Martín Parra, L. M., Matas, J., Andonaegui, P., & Fernández-Suárez, J. (2021). Geochemistry and Sm–Nd isotopic sources of late Ediacaran siliciclastic series in the Ossa–Morena complex: Iberian–bohemian correlations. *International Journal of Earth Sciences*, *110*, 467–485. https://doi.org/10.1007/s00531-020-01963-0

Rooney, T. P., & Riecker, R. E. (1969). *Experimental deformation of hornblende and amphibolite*. (air force Cambridge research laboratories, Ed.), *Enviromental research papers* (Vol. *299*).

Rooney, T. P., Riecker, R. E., & Gavasci, A. T. (1975). Hornblende deformation features. *Geology*, *3*, 364–366. https://doi.org/10.1130/0091-7613(1975)3<364:HDF>2.0.CO;2

Ryan, W. B. F., Carbotte, S. M., Coplan, J. O., O'Hara, S., Melkonian, A., Arko, R., Weissel, R. A., Ferrini, V., Goodwillie, A., Nitsche, F., Bonczkowski, J., & Zemsky, R. (2009). Global multi-resolution topography synthesis. *Geochemistry, Geophysics, Geosystems*, *10*, Q03014. https://doi.org/10.1029/2008GC002332

Saka, H., Goto, D., & Moon, W. J. (2008). Dislocations in plastically deformed apatite. *Journal of Materials Science*, *43*, 3234–3239. https://doi.org/10.1007/s10853-008-2551-z

Sánchez-García, T., Quesada, C., Bellido, F., Dunning, G. R., & González del Tánago, J. (2008). Two-step magma flooding of the upper crust during rifting: The Early Paleozoic of the Ossa Morena Zone (SW Iberia). *Tectonophysics*, *461*(1–4), 72–90. https://doi.org/10.1016/j.tecto.2008.03.006

Sánchez-Lorda, M. E., Ábalos, B., García de Madinabeitia, S., Eguíluz, L., Gil Ibarguchi, J. I., & Paquette, J. L. (2016). Radiometric discrimination of pre-Variscan amphibolites in the Ediacaran Serie Negra (Ossa-Morena zone, SW Iberia). *Tectonophysics*, *681*, 31–45. https://doi.org/10.1016/j.tecto.2015.09.020

Sánchez-Lorda, M. E., Sarrionandia, F., Ábalos, B., Carrracedo, M., Eguíluz, L., & Gil Ibarguchi, J. I. (2014). Geochemistry and paleotectonic setting of Ediacaran metabasites from the Ossa-Morena zone (SW Iberia). *International Journal of Earth Sciences*, *103*, 1263–1286. https://doi.org/10.1007/s00531-013-0937-x

Sarrionandia, F., Ábalos, B., Errandonea-Martin, J., Eguíluz, L., Santos-Zalduegui, J. F., García de Madinabeitia, S., Carracedo-Sánchez, M., & Gil Ibarguchi, J. I. (2020). Ediacaran - earliest Cambrian arc-tholeiite and adakite associations of the Malcocinado formation (Ossa-Morena zone, SW Spain): Juvenile continental crust and deep crustal reworking in northern Gondwana. *Lithos*, *372–373*, 105683. https://doi.org/10.1016/j.lithos.2020.105683

Schäfer, H.-J. (1990). Geochronological investigations in the Ossa Morena zone, SW Spain. PhD. Dissertation. Eidgenössische Technische Hoschschule, Zürich, Switzerland.

Schäfer, H. J., Gebauer, D., & Nägler, T. F. (1991). Evidence for Silurian eclogite- and granulite facies metamorphism in the Badajoz–Córdoba shear belt, SW Spain. *Terra abstracts Suppl. 6 to Terra Nova, 3, 11*.

Schäfer, H. J., Gebauer, D., Nägler, T. F., & Von Quadt, A. (1988). U-Pb zircon and Sm-Nd studies of various rock-types of the Ossa-Morena zone (Southwest Spain). Simposio Sobre Cinturones Orogénicos, I Congreso Español de Geología, 51–57.

Schäfer, H. J., Nägler, T. F., & Gebauer, D. (1989). Pan-African and Caledonian ages in the Ossa-Morena zone (Southwest Spain): A U-Pb zircon and Sm-Nd study. *Terra Abstracts*, *1*, 350–351.

Schwartz, S., Guillot, S., Reynard, B., Lafay, R., Debret, B., Nicollet, C., Lanari, P., & Auzende, A. L. (2013). Pressure-temperature estimates of the lizardite/antigorite transition in high pressure serpentinites. *Lithos*, *178*, 197–210. https://doi.org/10.1016/j.lithos.2012.11.023

Silva, J. B., & Pereira, M. F. (2004). Transcurrent continental tectonics model for the Ossa-Morena zone Neoproterozoic-Paleozoic evolution, SW Iberian massif, Portugal. *International Journal of Earth Sciences*, *93*, 886–896. https://doi.org/10.1007/s00531-004-0424-5

Simancas, J. F., Galindo-Zaldívar, J., & Azor, A. (2000). Three-dimensional shape and emplacement of the Cardenchosa deformed pluton (Variscan Orogen, southwestern Iberian massif). *Journal of Structural Geology*, *22*, 489–503. https://doi.org/10.1016/S0191-8141(99)00178-9

Simancas, J. F., Poyatos, D. M., Expósito, I., Azor, A., & González Lodeiro, F. (2001). The structure of a major suture zone in the SW Iberian massif: The Ossa-Morena/central Iberian contact. *Tectonophysics*, *332*, 295–308. https://doi.org/10.1016/S0040-1951(00)00262-6

Skrotzki, W. (1992). Defect structure and deformation mechanisms in naturally deformed hornblende. *Physica Status Solidi (A)*, *131*, 605–624. https://doi.org/10.1002/pssa.2211310232

Soda, Y., & Wenk, H. R. (2014). Antigorite crystallographic preferred orientations in serpentinites from Japan. *Tectonophysics*, *615–616*, 199–212. https://doi.org/10.1016/j.tecto.2013.12.016

Solís-Alulima, B., López-Carmona, A., & Abati, J. (2020). Ordovician metamorphism and magmatism preserved in the Ossa Morena complex: SHRIMP geochronology, geochemistry and Sr–Nd isotopic signatures of the Sierra Albarrana domain (SW Iberian massif). *Lithos*, *374–375*, 105700. https://doi.org/10.1016/j.lithos.2020.105700

Tamblyn, R., Zack, T., Schmitt, A. K., Hand, M., Kelsey, D., Morrissey, L., Pabst, S., & Sarov, I. P. (2019). Blueschist from the Mariana forearc records long-lived residence of material in the subduction channel. *Earth and Planetary Science Letters*, *519*, 171–181. https://doi.org/10.1016/j.epsl.2019.05.013

Tornos, F., Inverno, C. M. C., Casquet, C., Mateus, A., Ortiz, G., & Oliveira, V. (2004). The metallogenic evolution of the Ossa-Morena zone. *Journal of Iberian Geology*, *30*, 143–181.

Van De Moortèle, B., Bezacier, L., Trullenque, G., & Reynard, B. (2010). Electron back-scattering diffraction (EBSD) measurements of antigorite lattice-preferred orientations (LPO). *Journal of Microscopy*, *239*, 245–248. https://doi.org/10.1111/j.1365-2818.2010.03398.x

Vermeesch, P. (2018). IsoplotR: A free and open toolbox for geochronology. *Geoscience Frontiers*, *9*, 1479–1493. https://doi.org/10.1016/j.gsf.2018.04.001

Vollmer, F. W. (1990). An application of eigenvalue methods to structural domain analysis. *Geological Society of America Bulletin*, *102*, 786–791. https://doi.org/10.1130/0016-7606(1990)102<0786:AAOEMT>2.3.CO;2

von Raumer, J. F., Stampfli, G. M., Arenas, R., & Sánchez Martínez, S. (2015). Ediacaran to Cambrian oceanic rocks of the Gondwana margin and their tectonic interpretation. *International Journal of Earth Sciences*, *104*, 1107–1121. https://doi.org/10.1007/s00531-015-1142-x

Wakabayashi, J. (2017). Serpentinites and serpentinites: Variety of origins and emplacement mechanisms of serpentinite bodies in the California Cordillera. *Island Arc*, *26*, e12205. https://doi.org/10.1111/iar.12205

Wang, X., Zeng, Z., & Chen, J. (2009). Serpentinization of peridotites from the southern Mariana forearc. *Progress in Natural Science*, *19*, 1287–1295. https://doi.org/10.1016/j.pnsc.2009.04.004

Whitney, D. L., & Evans, B. W. (2010). Abbreviations for names of rock-forming minerals. *American Mineralogist*, *95*, 185–187. https://doi.org/10.2138/am.2010.3371

Wicks, F. J., & Whittaker, E. J. (1977). Serpentine textures and serpentinization. *Canadian Mineralogist*, *15*, 459–488.

Wu, L., Murphy, J. B., Quesada, C., Li, Z.-X., Waldron, J. W. F., Williams, S., Pisarevsky, S., & Collins, W. J. (2020). The amalgamation of Pangea: Paleomagnetic and geological observations revisited. *GSA Bulletin*, *133*, 625–646. https://doi.org/10.1130/b35633.1

Zhang, X. L., Hu, L., Ji, M., Liu, J. L., & Song, H. L. (2013). Microstructures and deformation mechanisms of hornblende in Guandi complex, the Western Hills, Beijing. *Science China Earth Sciences*, *56*, 1510–1518. https://doi.org/10.1007/s11430-013-4636-z

SUPPORTING INFORMATION

Additional supporting information can be found online in the Supporting Information section at the end of this article.

Appendix S1. Description of the methods used for rock-forming mineral identification (petrographic thin sections, X-ray diffraction, Raman spectroscopy), mineral geochemical analysis (electron-microprobe), determination of mineral petrofabric (electron back-scattered diffraction, EBSD), and apatite dating (laser ablation inductively coupled plasma mass spectrometry, LA-Q-ICPMS).

Table S1. Geographic coordinates of the location of studied samples and brief descriptions of lithotypes and the mineral content identified through X-Ray Diffraction.

Table S2. Microprobe mineral geochemical data and structural formula calculations for chlorite, amphibole, talc, ilmenite, magnetite and apatite from the samples studied.

Table S3. LA-Q-ICP-MS results obtained for apatite. All values are only corrected for fractionation with matrix matching standards (see analytical methods for further details). U and Pb contents are estimations obtained by comparison with MAD apatite standards.

How to cite this article: Ábalos, B., Puelles, P., & Gil Ibarguchi, J. I. (2023). Polyphase tectonic reworking of serpentinites and chlorite-tremolite-talc rocks (SW Spain) from the subduction forearc to intracontinental emplacement. *Journal of Metamorphic Geology*, *41*(4), 491–523. https://doi.org/10.1111/jmg.12704